

Single hydroxo-bridged group 13 metalloporphyrin dimers: Solution studies and solid-state structures

Orde Q. Munro^{*a,c}, Athanassios G. Coutsolelos^{*b,c}, Beisong Cheng^c
and W. Robert Scheidt^{*c}

^a School of Chemistry, University of the Witwatersrand, Johannesburg, PO WITS 2050, South Africa

^b Department of Chemistry, University of Crete, Voutes Campus, 70013 Heraklion-Crete, Greece

^c Department of Chemistry and Biochemistry, University of Notre Dame, Notre Dame, Indiana 46556, USA

Received 5 June 2019

Accepted 15 July 2019

ABSTRACT: The syntheses of indium, gallium and aluminum porphyrin dimers with a single hydroxo-bridge, $\{[M(\text{Porph})]_2(\text{OH})\}^+$, are described. Emphasis is given to indium and gallium derivatives. The X-ray structures for $\{[\text{Ga}(\text{OEP})]_2(\text{OH})\}\text{ClO}_4$ and $\{[\text{In}(\text{OEP})]_2(\text{OH})\}\text{ClO}_4$ (two forms) are presented. The dimeric molecules can be synthesized by the acid-treatment of the corresponding hydroxo-ligated monomeric complexes $[\text{M}(\text{OEP})(\text{OH})]$ and $[\text{M}(\text{TPP})(\text{OH})]$. The nature of the starting material (the hydroxo-ligated monomer) was first suggested by IR spectroscopy and further proved by proton-deuterium exchange followed by ^1H NMR spectroscopy. The structure of a monomeric indium hydroxide complex, $[\text{In}(\text{OEP})(\text{OH})]$, is also presented. The synthesis of the dimer for all metals can be monitored by UV-vis spectroscopy, which clearly demonstrates that a blue-shift of the Soret band accompanies formation of the dimer from the monomer. A strong π - π interaction between the two porphyrin rings of these μ -hydroxo-bridged dimers is confirmed both by solution state studies (^1H NMR and UV-vis spectroscopy) and the X-ray structures of $\{[\text{M}(\text{OEP})]_2(\text{OH})\}\text{ClO}_4$ ($\text{M} = \text{In}, \text{Ga}$). In addition, exposure of methylene chloride solutions of these bridged complexes to white light afforded the corresponding chloro derivatives, $[\text{M}(\text{Porph})\text{Cl}]$. The stereochemistry of a range of μ -hydroxo dimers is discussed and DFT simulations at the HSEH1PBE/SDD level of theory provide suitable structural models and further electronic structure insights on selected $[\text{Ga}(\text{Porph})(\text{OH})]$ and $\{[\text{Ga}(\text{Porph})]_2(\text{OH})\}^+$ derivatives.

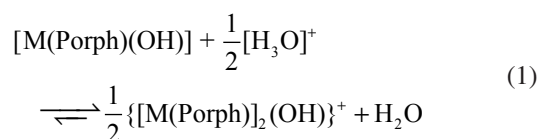
KEYWORDS: group 13 metalloporphyrin, hydroxo dimer, condensation, X-ray crystallography, DFT.

INTRODUCTION

A number of strategies have been described for the formation of metalloporphyrin dimers linked by a bridging group. These include (1) complexes of the type $\text{M}(\text{Porph})(\text{Porph}')$, where $\text{Porph} = \text{or} \neq \text{Porph}'$ and M is a polyvalent metal ion from the lanthanide or actinide series that serves as the bridging group between the macrocycles [1]–[6], and (2) dimers with the molecular formula $(\text{Porph})\text{M}-\text{M}'(\text{Porph}')$, where $\text{Porph} = \text{or} \neq \text{Porph}'$, $\text{M} = \text{or} \neq \text{M}'$, and a metal–metal bond links the monomers [7, 8]. We have recently reported

the syntheses and structural characterization of another class of metalloporphyrin dimers in which the two porphyrins are linked by a single μ -hydroxo bridge (Fig. 1), including $\{[\text{Fe}(\text{OEP})]_2(\text{OH})\}\text{ClO}_4$ [9, 10], $\{[\text{Mn}(\text{OEP})]_2(\text{OH})\}\text{ClO}_4$ [11], and $\{[\text{Mn}(\text{TPP})]_2(\text{OH})\}\text{ClO}_4$ [12].

All of these $\text{M}(\text{III})$ μ -hydroxo dimers have been obtained by the stoichiometric proton-dependent *condensation* of their corresponding monomeric hydroxo complexes (Eq. 1),



* Correspondence to: Orde Q. Munro, email, Orde.Munro@wits.ac.za; Athanassios G. Coutsolelos, email, acoutsol@uoc.gr; W. Robert Scheidt, email; Scheidt@nd.edu.

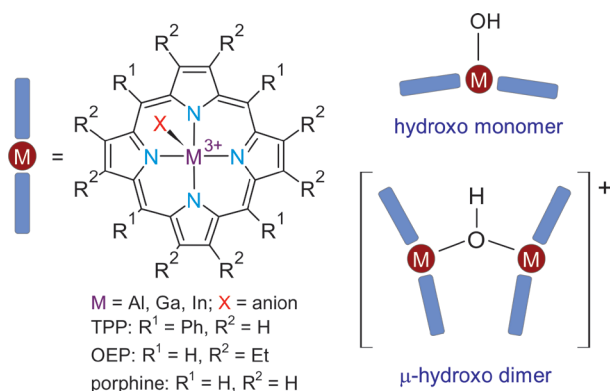


Fig. 1. Metalloporphyrin structures and a schematic illustration of the geometries of the 5-coordinate hydroxo monomers and μ -hydroxo dimers described in this work

We have found that $\{[\text{Fe}(\text{OEP})_2(\text{OH})]\text{ClO}_4\}$ may also be prepared by *protonation* of the μ -oxo species, $[\text{Fe}(\text{OEP})_2\text{O}]$ [9, 13]. Rath and co-workers have extended the iron studies with a number of different porphyrins and counterions [14].

As a continuation of our study of this novel class of dimeric metalloporphyrin derivatives, we have synthesized main group trivalent μ -hydroxo dimers to test the generality of the synthetic method and to compare the chemical behavior of these systems with that of their transition metal counterparts. We have also studied the solution structures of $\{[\text{Ga}(\text{OEP})_2(\text{OH})]\text{ClO}_4\}$ and $\{[\text{Ga}(\text{TPP})_2(\text{OH})]\text{ClO}_4\}$ using ^1H NMR, ^{13}C NMR, and ^{71}Ga NMR spectroscopy. The dynamic structures of these diamagnetic dimers are compared with their X-ray structures. Solid state structural data are provided by

the low-temperature X-ray structure of the gallium(III) and indium(III) derivatives $\{[\text{M}(\text{OEP})_2(\text{OH})]\text{ClO}_4\}$. The preparation and crystal structure of two additional Group 13 hydroxo-bridged species have been reported in the literature [15], however, the gallium derivative differs from all other species described herein, with one of the two gallium centers coordinated to a water molecule to form a six-coordinate species. DFT simulations at the HSEH1PBE/SDD level of theory both *in vacuo* and in a chloroform solvent continuum were used to model the structures of selected $\{[\text{Ga}(\text{Porph})]_2(\text{OH})\}^+$ derivatives, their electronic spectra, and their NMR shielding parameters. Selected DFT-calculated properties are reported alongside the experimental data where relevant to facilitate insightful comparisons. A deeper understanding of the relationship between molecular and electronic structure and the spectroscopic behavior of this class of compounds has consequently been achieved.

RESULTS

NMR Spectroscopy

The temperature dependence of the 1D ^1H and $^{13}\text{C}\{^1\text{H}\}$ spectra for the hydroxide-bridged complexes $\{[\text{Ga}(\text{OEP})_2(\text{OH})]\text{ClO}_4\}$ and $\{[\text{Ga}(\text{TPP})_2(\text{OH})]\text{ClO}_4\}$ revealed that both are stable over the range of -40 to $+90^\circ\text{C}$. The hydroxide bridge protons of these two gallium porphyrin derivatives resonate in the high field region between -12.5 to -15.0 ppm. The presence of the OH bridge was further supported by the fact that after the addition of a drop of D_2O to the solutions, the high field signal corresponding to one proton disappeared due

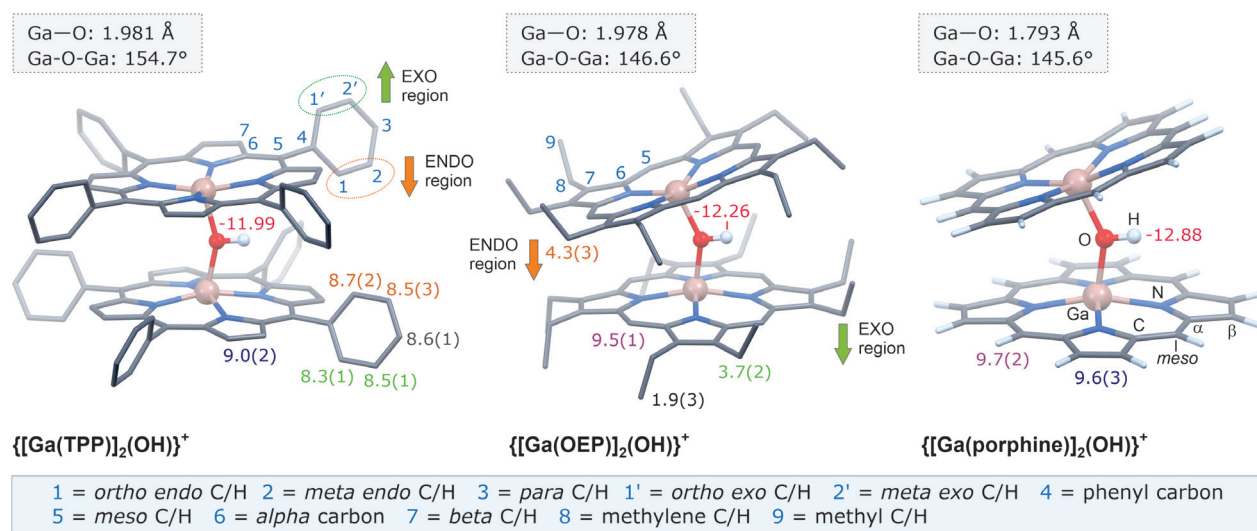


Fig. 2. Illustration of the different molecular regions, protons, and carbon atoms relevant to interpreting the NMR spectra of $\{[\text{Ga}(\text{Porph})]_2(\text{OH})\}^+$ derivatives. Hydrogen atoms appended to carbon have been omitted from the DFT-calculated structures where necessary for clarity. DFT-calculated chemical shifts (CHCl_3 solvent continuum, $\delta_{\text{H}}^{\text{calc}}$), are in ppm. Selected bond angles and bond distances for the solution phase structures are indicated

Table 1. ^1H NMR chemical shifts, δ_{H} (ppm), for hydroxo-bridged Ga(III) porphyrin dimers and their monomeric precursors measured in CDCl_3 solution at ambient temperature. DFT-calculated chemical shifts for the dimers are given in Fig. 2

Complex	<i>beta</i>	<i>meso</i>	<i>ortho</i>		<i>meta</i>		<i>para</i>	CH_2	CH_3	OH
			<i>endo</i>	<i>exo</i>	<i>endo</i>	<i>exo</i>				
$\{[\text{Ga}(\text{OEP})]_2(\text{OH})\}\text{ClO}_4$		9.36						4.024/4.16	1.70	-13.87
$[\text{Ga}(\text{OEP})(\text{OH})]$		10.30						4.17	1.97	-7.18
$\{[\text{Ga}(\text{TPP})]_2(\text{OH})\}\text{ClO}_4^{\text{a}}$	8.64		8.05	7.64	7.82	7.64	7.85			-14.51
			<i>ortho</i>		<i>meta, para</i>					
$[\text{Ga}(\text{TPP})(\text{OH})]$	9.06		8.11/8.39		8.12					-6.63

^aRecorded at -20.0°C .

to the rapid exchange between hydrogen and deuterium (Supporting Information, Fig. S1). The OH protons of the monomeric precursors $[\text{Ga}(\text{OEP})(\text{OH})]$ and $[\text{Ga}(\text{TPP})(\text{OH})]$ resonate at about 7 ppm to lower field. The expected chemical and magnetic environments (regions) for the protons of the μ -OH species are shown using the DFT-calculated geometries (CHCl_3 solvent continuum) of the complexes in Fig. 2.

The solution structure and dynamics of the hydroxo-bridged gallium OEP and TPP derivatives were studied in detail by NMR methods over the temperature range -20 to $+20^\circ\text{C}$. It was found that all phenyl groups in the TPP derivative and all ethyl groups in the OEP derivative are magnetically equivalent. However, all individual protons and carbons of a phenyl group give rise to the separate resonances, *i.e.* they are magnetically nonequivalent. Furthermore, the methylene protons of the ethyl groups of $\{[\text{Ga}(\text{OEP})]_2(\text{OH})\}\text{ClO}_4$ were found to be anisochronous. The pyrrolic and *meso* protons exhibited single resonance lines for the TPP and OEP derivatives, respectively. The proton resonances for both hydroxo-bridged gallium porphyrins and their corresponding precursors were unambiguously assigned to individual hydrogen atoms based on the interpretation of the DQF-COSY and NOESY spectra (Table 1). The signals of all carbons with directly attached protons were assigned by analyzing HETCOR spectra. Assignments of signals derived from quaternary carbon nuclei are based on their chemical shifts. The ^{13}C chemical shifts are summarized in Table S1.

^{13}C spin-lattice relaxation times, T_1 , and NOE enhancements were measured for carbons with directly attached protons at a magnetic field strength B_0 of 11.74 T (125.69 MHz, ^{13}C) for $\{[\text{Ga}(\text{OEP})]_2(\text{OH})\}\text{ClO}_4$ and $\{[\text{Ga}(\text{TPP})]_2(\text{OH})\}\text{ClO}_4$ over the temperature range of -20 to $+20^\circ\text{C}$. Both the relaxation times, T_1 , (Table S2) and NOE parameters (Table S3) of all measured carbons increased with temperature. The values of the NOE parameters for $\{[\text{Ga}(\text{TPP})]_2(\text{OH})\}\text{ClO}_4$, however, did not reach their theoretical maximum of 1.988 at temperatures below 0°C .

1D ^{71}Ga NMR spectra (ambient temperature) were measured for the μ -hydroxo-bridged gallium(III) porphyrin dimers and their five-coordinate hydroxo precursors. Only the precursor complexes, $[\text{Ga}(\text{OEP})(\text{OH})]$ and $[\text{Ga}(\text{TPP})(\text{OH})]$, afforded observable resonance signals in the spectrum at 72.8 and 77.1 ppm, respectively.

Mass spectrometry

The molecular formula, $\{[\text{Ga}(\text{Porph})]_2(\text{OH})\}\text{ClO}_4$, for this class of hydroxo-bridged metalloporphyrins was confirmed by mass spectrometry. The molecular ion peaks observed for both dinuclear complexes corresponds to the entity $[\text{Ga}(\text{Porph})]_2(\text{OH})^+$, with relative intensities of 22% and 1% for the OEP and TPP derivatives, respectively. The fragmentation patterns of these dimeric gallium(III) derivatives are intrinsically similar to the patterns observed for the porphyrin free bases. The expected isotopic composition (comprising the isotopes ^{69}Ga and ^{71}Ga) of the bimetallic compound was confirmed in each case.

Electrochemistry

Electrochemical studies of $\{[\text{Ga}(\text{OEP})]_2(\text{OH})\}\text{ClO}_4$ and $\{[\text{Ga}(\text{TPP})]_2(\text{OH})\}\text{ClO}_4$ were carried out under argon in CH_2Cl_2 containing 0.1 M TBAP as the supporting electrolyte. It is to be noted that dissolution of the μ -hydroxo dimers in the electrochemical solvent mixture ($\text{CH}_2\text{Cl}_2/0.1$ M TBAP) favored *partial* dissociation of the dimer. (This observation was confirmed by UV-vis spectroscopy). The dissociation equilibrium was observed for both the dinuclear OEP and TPP derivatives. However, the extent of dissociation in pure organic solvents was negligible. Otherwise, the complexes are stable on the cyclic voltammetry time-scale and no loss of the μ -hydroxo bridge was detected during oxidation cycles.

Table 2 summarizes the electrochemical data for the gallium(III) complexes investigated. The $E_{1/2}$ for the first reduction in CH_2Cl_2 measured -1.43 V for $\{[\text{Ga}(\text{TPP})]_2(\text{OH})\}\text{ClO}_4$, while the OEP congener was reduced at -1.77 V. The second reduction in CH_2Cl_2

Table 2. Half-wave peak potentials (V vs. SCE) of μ -OH dimers and their monomeric precursors in CH_2Cl_2 (0.1 M TBAP) at ambient temperature

Complex	Oxidation		Reduction	
	2nd	1st	1st	2nd
$\{[\text{Ga}(\text{TPP})_2(\text{OH})]\text{ClO}_4$	1.34	1.08	-1.04	-1.43
$[\text{Ga}(\text{TPP})(\text{OH})]^a$	1.42	1.18	-1.16	-1.54
$\{[\text{Ga}(\text{OEP})_2(\text{OH})]\text{ClO}_4$	1.31	1.04	-1.32	-1.77
$[\text{Ga}(\text{OEP})(\text{OH})]^a$	1.44	1.01	-1.37	-1.88

^aSimilar data are available in the literature for these complexes [16].

ranges from -1.04 V for $\{[\text{Ga}(\text{TPP})_2(\text{OH})]\text{ClO}_4$ to -1.32 V for $\{[\text{Ga}(\text{OEP})_2(\text{OH})]\text{ClO}_4$. Two reversible oxidations were observed for both $\{[\text{Ga}(\text{OEP})_2(\text{OH})]\text{ClO}_4$ and $\{[\text{Ga}(\text{TPP})_2(\text{OH})]\text{ClO}_4$ (refer to Table 2).

X-ray crystallography

The crystal structures of five-coordinate Group 13 metalloporphyrins with hydroxide as the axial ligand have been determined and are reported here. The structures are those of the monomeric hydroxide $[\text{In}(\text{OEP})(\text{OH})]$ (Supporting Information, Fig. S6) and the dinuclear salts $\{[\text{Ga}(\text{OEP})_2(\text{OH})]\text{ClO}_4$ and $\{[\text{In}(\text{OEP})_2(\text{OH})]\text{ClO}_4$, which are the primary focus of our current structural studies. Two different crystalline forms (monoclinic and triclinic) of the indium species have been characterized. The structures of the dinuclear cations $\{[\text{Ga}(\text{OEP})_2(\text{OH})]^+$ and $\{[\text{In}(\text{OEP})_2(\text{OH})]^+$ (monoclinic polymorph) are shown in Fig. 3. The triclinic polymorph of $\{[\text{In}(\text{OEP})_2(\text{OH})]\text{ClO}_4$ had two independent molecules in the asymmetric unit; the structures of the unique cations are shown in Fig. 4. The salient structural feature in each case is the bent geometry of the M–(OH)–M bridge, which exceeds 140° and clearly cants the porphyrin rings within the dimer toward one another such that the separation between the ring edges measures between 3.3–3.5 Å.

The five-coordinate geometry of the metal ion results in a typical square pyramidal coordination group for each of the μ -hydroxo dimers, with perpendicular displacements of the metal ion from the 24-atom porphyrin mean plane ranging from 0.32 Å (Ga) to 0.66 Å (In). The displacement vector, in all cases, is toward the bridging hydroxyl group and the porphyrins adopt domed conformations. Primarily because of the larger ionic radius of In(III) (0.94 Å) compared with Ga(III) (0.76 Å) [17], the M...M separation in the indium dimers (3.927–3.966 Å) exceeds that for the gallium derivative (3.677 Å). The mean M–O (2.093 (7) Å) and M–N_p (2.134 (4) Å) bond distances for the indium derivatives structurally elucidated here are consequently also longer than those of the gallium derivative (1.911 (0) Å and 2.019 (2) Å, respectively).

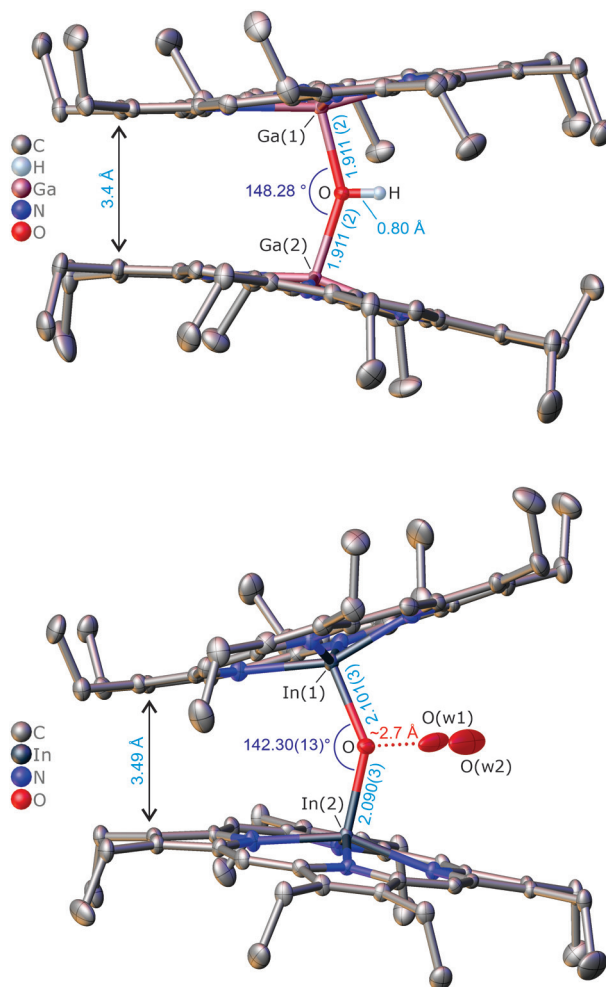


Fig. 3. Edge-on thermal ellipsoid views of the cations of $\{[\text{Ga}(\text{OEP})_2(\text{OH})]\text{ClO}_4$ and $\{[\text{In}(\text{OEP})_2(\text{OH})]\text{ClO}_4$ (monoclinic form). Atoms are contoured at the 50% probability level. Hydrogen atoms have been omitted for clarity, except for the hydrogen atom of the μ -hydroxo bridging group in the gallium derivative. The hydrogen atom in the indium derivative was not located experimentally in the E map, but the $\text{O}\cdots\text{O}$ (water) distance is consistent with the presence of a hydrogen bond between the hydroxide ion H atom donor and a solvate water O atom acceptor. For simplicity, the ClO_4^- counterions are not shown

DFT simulations

We have used DFT simulations at the HSEH1PBE/SDD level of theory to provide some theoretical insight on the experimental structures, electrochemical data, and spectroscopic features (NMR and UV-vis spectroscopy) of the Ga(III) μ -hydroxo dimers investigated here. An exhaustive treatise on all of the DFT-calculated parameters for the compounds is beyond the scope of the present article.

Molecular structures. The structures of $[\text{Ga}(\text{Porph})(\text{OH})]$ and $\{[\text{Ga}(\text{Porph})_2(\text{OH})]^+$, where Porph = TPP and OEP, as well as $[\text{Ga}(\text{OEP})(\text{OH}_2)_2]^+$, were calculated both *in vacuo* and in a chloroform solvent continuum. Several

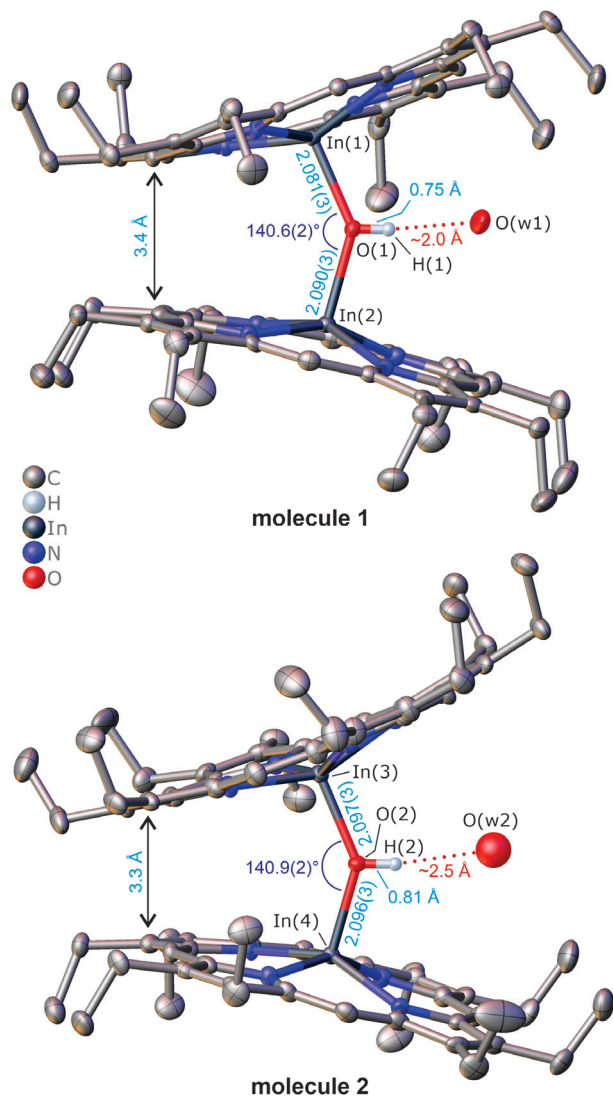


Fig. 4. Edge-on thermal ellipsoid views of the two independent cations of $\{[\text{In}(\text{OEP})_2(\text{OH})]\text{ClO}_4$ (triclinic polymorph). Atoms are contoured at the 50% probability level. Hydrogen atoms have been omitted for clarity, except for the hydrogen atom of the μ -hydroxo bridging groups. For simplicity, the ClO_4^- counterions are not shown

simulations were also effected in a dichloromethane solvent continuum to facilitate direct comparison with experimental electronic spectra. Representative solution phase structures of the μ -hydroxo dimers are shown in Fig. 2; key structural and electronic parameters for the complexes are summarized in Table 3. The solution phase structure of $\{[\text{Ga}(\text{OEP})_2(\text{OH})]^+\}$ is broadly consistent with the X-ray structure of the complex, displaying the same characteristic 5-coordinate metal ion geometry, canted porphyrin rings, domed macrocycle conformations, and intramolecular ring...ring contacts. The solution phase conformations of the TPP and porphine μ -hydroxo dimers are generally similar, though intramolecular steric repulsion effects in the TPP derivative evidently result in a near

parallel arrangement for the porphyrin rings. The increase in steric bulk of the porphyrin ring substituents underpins the increase in the $\text{Ga}\cdots\text{Ga}$ distance from 3.77 Å in the porphine derivative to 3.87 Å in the TPP derivative (Fig. S9). The hallmark coordination group parameters of the DFT-calculated structure of $\{[\text{Ga}(\text{OEP})_2(\text{OH})]^+\}$ in a chloroform solvent continuum ($\text{Ga}-\text{O}$, $\text{Ga}-\text{O}-\text{Ga}$, and $\text{Ga}-\text{N}_p$) are within 2–13% of their experimental values (X-ray crystallography), offering a measure of confidence in the DFT method and basis set used in this study (taking into account the effect of the solvent continuum). One noteworthy difference is the out-of-plane displacement of the metal ion, $\Delta\text{M}24$, which measures 0.439 (1) Å for the solution phase structure of $\{[\text{Ga}(\text{OEP})_2(\text{OH})]^+\}$ and is significantly larger than that observed crystallographically (0.32 Å). This accounts for the longer $\text{Ga}-\text{N}_p$ distance in the solution structure (2.047 (14) Å) compared with the X-ray structure (2.019 (1) Å) and likely reflects the lack of axial compression of the μ -hydroxo dimer in the CHCl_3 solvent continuum (*i.e.* the absence of crystal packing constraints).

FMOs and electronic spectra. The four frontier MOs (FMOs) of $\{[\text{Ga}(\text{OEP})_2(\text{OH})]^+\}$ are shown in Fig. 5. All four FMOs evenly span both porphyrin rings in the dimer despite the lack of any true symmetry elements in the complex. The Ga(III) ions are positioned at nodes in the MO wave functions and no components of the four FMOs are located on the μ -hydroxo bridge. The HOMO and HOMO–1 are π -symmetry MOs that correspond to two non-degenerate wave functions of similar character that match the classical a_{1u} MO of a D_{4h} -symmetry metalloporphyrin [18–20]. The FMO energy gap ΔE_{FMO} ($E_{\text{LUMO}}-E_{\text{HOMO}}$) is significantly affected by the presence of the solvent, which modulates the splitting relative to the gas phase value, as evidenced by the ΔE_{FMO} data for $\{[\text{Ga}(\text{OEP})_2(\text{OH})]^+\}$ *in vacuo*, in CHCl_3 , and in CH_2Cl_2 (2.394, 1.781, and 2.410 eV, respectively).

The porphyrin ring substituent groups and nature of the species (monomeric five-coordinate hydroxo complex *vs.* μ -hydroxo dimer), however, have by far the largest effect on the electronic spectra of the complexes. In all cases, the Soret band shifts to a shorter wavelength for the μ -hydroxo dimer relative to the 5-coordinate hydroxo monomer (see Fig. S7). From Table 3, the OEP derivative exhibits the largest blue shift ($\Delta\lambda \sim 45$ nm), with the TPP derivative displaying a more modest shift of 14 nm. Also noteworthy is the calculated energy order of the substituent effect. Specifically λ_{max} follows the order $\text{OEP} < \text{porphine} < \text{TPP}$ for this series of Ga(III) hydroxo monomers and dimers, with the effect being especially pronounced in the μ -hydroxo dimers (the Soret band of the OEP derivative is blue-shifted by 38 nm relative to the TPP derivative). Significantly, the DFT-calculated spectra have allowed us to assign various experimentally-observed solution phase species with confidence, facilitating confirmation of the mechanistic pathway proposed for the synthesis of the μ -hydroxo dimers reported

Table 3. DFT-calculated structural and electronic parameters for monomeric and dimeric Ga(III) porphyrins in solution (chloroform solvent continuum)

Parameter	[Ga(TPP)(OH)]	{[Ga(TPP)] ₂ (OH)} ⁺	[Ga(OEP)(OH)]	{[Ga(OEP)] ₂ (OH)} ⁺	[Ga(P)(OH)] ^h	{[Ga(P)] ₂ (OH)} ⁺
Ga–N _p (Å) ^a	2.073 (12)	2.046 (17)	2.072 (11)	2.047 (14)	2.074 (10)	2.046 (13)
Ga–O (Å)	1.860 (0)	1.981 (0)	1.865 (0)	1.978 (0)	1.858 (0)	1.793 (0)
O–H (Å)	0.973	0.981	0.974	0.978	0.973	0.978
ΔM24 (Å) ^b	0.502	0.402 (1)	0.502	0.439 (1)	0.513	0.405 (0)
C···C (Å) ^c		4.41		3.62		3.60
Ga···Ga (Å)		3.87		3.79		3.77
N _p –Ga–O (°)	103 (2)	99 (8)	103 (2)	100 (6)	103 (2)	100 (5)
Ga–O–Ga (°)		154.7		146.6		145.6
N–Ga–Ga–N (ave, °) ^d		-29 (1)		-28.2 (7)		-34 (1)
24MP DA (°) ^e		5.5		18.0		19.1
δ _H (OH, ppm)	-5.47	-11.99	-5.96	-12.26	-6.01	-12.88
ν _{O-H} (cm ⁻¹) ^f	3799	3670	3794	3733	3801	3736
ν _{Ga-O} (cm ⁻¹)	553	559	549	550	555	557
ν _{Ga-Np} (cm ⁻¹)	391	393	364	356	374	396
ν _{Ga-O-H} (cm ⁻¹)	743	(755)	744	761	747	760
δ _{Ga-O-Ga} (cm ⁻¹)		368		386		396
H charge (OH) ^g	0.495	0.529	0.492	0.533	0.495	0.535
O charge (OH)	-1.203	-1.177	-1.205	-1.181	-1.203	-1.182
Ga charge	1.902	1.950	1.899	1.949	1.902	1.955
N _p charge (ave)	-0.727 (4)	-0.753 (6)	-0.733 (3)	-0.757 (5)	-0.735 (4)	-0.760 (5)
λ _{max} (Soret, nm)	396	382	379	334	371	349

^a N_p porphyrin nitrogen atom. ^b Perpendicular displacement of the metal ion from the 24-atom porphyrin mean plane. ^c Shortest C···C contact distance between porphyrin rings within the μ-hydroxo dimer. ^d Twist (torsion) angle based on the Ga–Np bond vectors between porphyrin rings within a μ-hydroxo dimer. ^e Dihedral angle between the 24-atom mean planes of each porphyrin ring within the dimer. ^f The appropriate scale factor for the IR vibrational frequencies is 0.964 (to give closer agreement with experimental ν_{O-H} data). ^g Fractional atomic charge calculated with the NBO model (in electron units). ^h P = porphine.

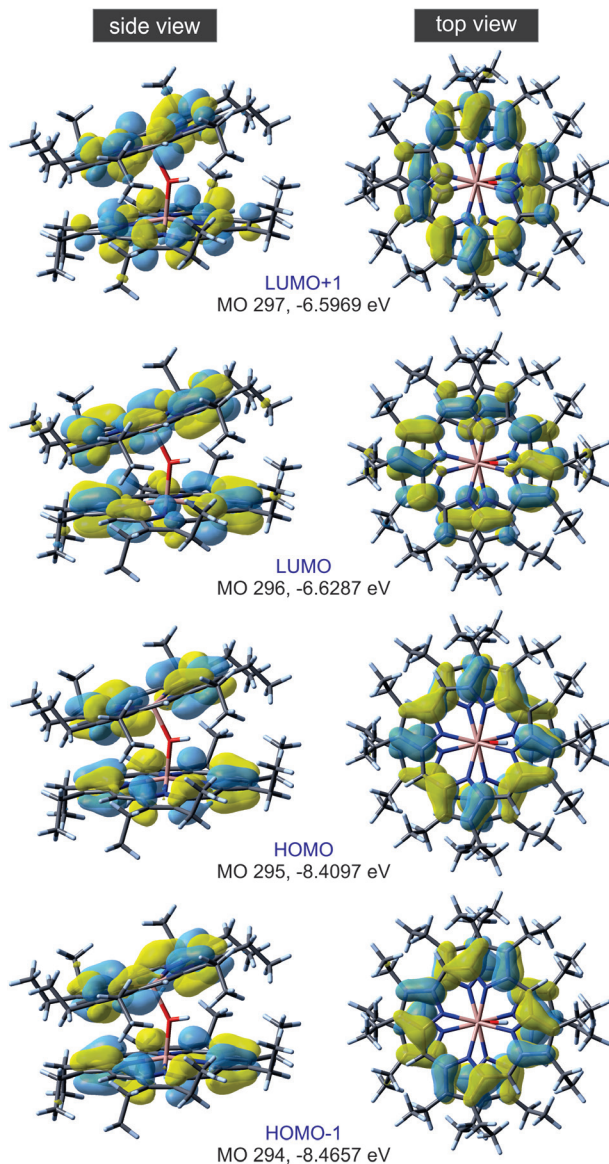


Fig. 5. Views of the frontier molecular orbitals (FMOs) for $\{[\text{Ga}(\text{OEP})_2(\text{OH})]^+\}$. The DFT-calculated structure represents the geometry of the cation optimized in a chloroform solvent continuum

here (this is discussed later in relation to Fig. 6). The relevant DFT-calculated electronic spectra of $[\text{Ga}(\text{OEP})(\text{OH})]$, $[\text{Ga}(\text{OEP})(\text{OH})_2]^+$, and $\{[\text{Ga}(\text{OEP})_2(\text{OH})]^+\}$ have been included alongside the experimental spectra in Fig. 8 to further facilitate our discussion of the synthesis of the present class of metalloporphyrin μ -hydroxo dimers.

NMR and electrostatic parameters. To compare the experimental and theoretical NMR chemical shift data, the calculated isotropic shieldings (GIAO method, CHCl_3 solvent continuum) of all chemically equivalent nuclei were averaged to remove magnetic inequivalences associated with the static nature of the geometry-optimized DFT structures. This procedure is akin to the

dynamic signal averaging that occurs experimentally. DFT-calculated proton chemical shift data for the gallium μ -hydroxo dimers are given in Fig. 2 along with the structures of the complexes.

Of particular interest, the calculated chemical shifts of the OH proton range from -5.47 ppm in $[\text{Ga}(\text{TPP})(\text{OH})]$ to -12.88 ppm in $\{[\text{Ga}(\text{P})_2(\text{OH})]^+\}$, consistent with the experimental trend that the bridged hydroxyl proton in the μ -hydroxo dimers experiences strongly enhanced shielding relative to the axial hydroxo ligand of the relevant five-coordinate monomer. The calculated OH proton chemical shifts are, however, less shielded by 1.1 – 1.6 ppm relative to the experimental data. (Although the largest deviations occur for the OH protons of the μ -hydroxo dimers, other proton chemical shifts are generally more accurately calculated.)

Calculated ^{13}C chemical shifts are tabulated alongside the experimental chemical shifts for the μ -hydroxo dimers in Table S1. The pyrrole β -C (135.2 – 146.9 ppm) and all substituent group chemical shifts are within 5 ppm of the experimental chemical shifts. The calculated pyrrole α -C chemical shifts (150.8 – 153.6 ppm) span a narrow range, but are more deshielded (by up to 8 ppm) relative to the experimental chemical shifts.

The fractional atomic charge distribution for the atoms of the coordination group was calculated with the NBO model (Table 3) [21] which gives results that are independent of the basis set used for the simulations. The mean charges on the hydroxyl group O atom (-1.19 ± 0.01), H atom ($+0.51 \pm 0.02$), and Ga(III) ion (1.93 ± 0.03) are essentially independent of the structure of the complex (monomer vs. μ -hydroxo dimer). The porphyrin nitrogen atoms (N_p) are similarly charged for all of the complexes (-0.74 ± 0.01), despite their differing peripheral substituent groups and the nature of the species (monomer vs. dimer). The μ -hydroxo dimers, however, all have slightly more negatively charged (~ 0.03 units) porphyrin nitrogen atoms relative to the five-coordinate hydroxo monomers.

DISCUSSION

Compound synthesis and electronic spectra

We have previously demonstrated the syntheses of a number of single μ -hydroxo bridged metalloporphyrin complexes including $\{[\text{Fe}(\text{OEP})_2(\text{OH})]\text{ClO}_4$ [9], $\{[\text{Mn}(\text{OEP})_2(\text{OH})]\text{ClO}_4$ [11], and $\{[\text{Mn}(\text{TPP})_2(\text{OH})]\text{ClO}_4$ [12], through the *condensation* of their corresponding monomeric aqua complexes rather than the *protonation* of their unprotonated μ -oxo forms. As a continuation of our studies on monomeric and dimeric congeners within this broad class of compounds, we carried out the analogous syntheses with trivalent Group 13 metalloporphyrins to test the generality of such a synthetic method, as well as to compare their chemical behavior. Figure 6 summarizes our approach to the

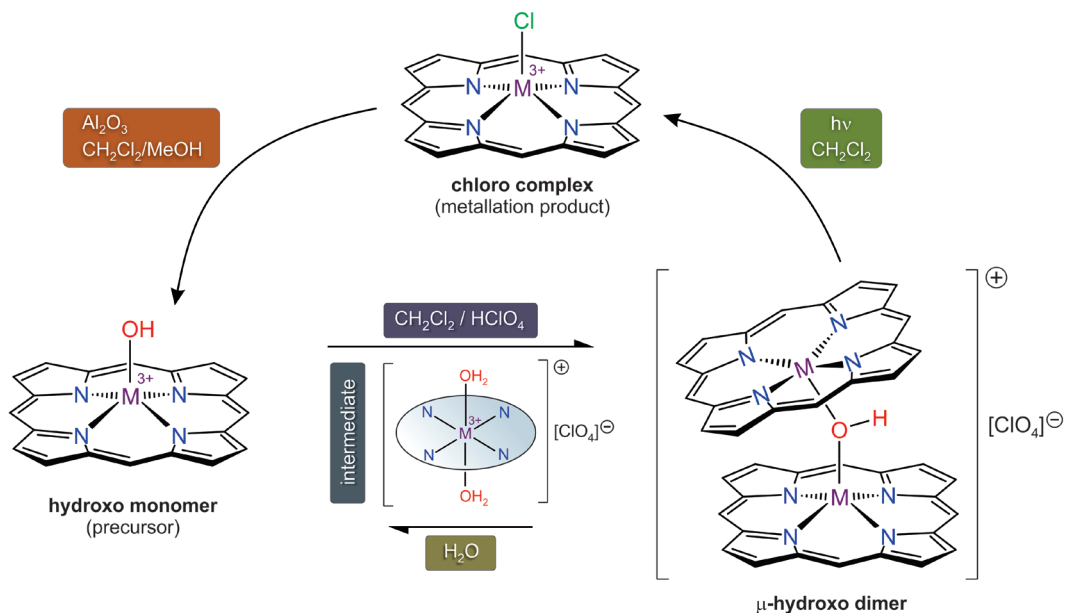


Fig. 6. Reaction scheme summarizing the interconversion pathways between five-coordinate Group 13 metalloporphyrin species ($M = \text{Al, Ga, In}$). Porphyrin substituents have been omitted for clarity. Species assignments are readily made from the electronic spectra of the compounds

synthesis of these μ -hydroxo-bridged metalloporphyrin dimers, the postulated reaction intermediate, and the behavior of the dimers toward white light.

In the reaction mixture (acidified solution) the equilibrium between the monomeric 5-coordinate hydroxo species and the μ -hydroxo dimer is strongly dependent on the amount of HClO₄ present (Eq. 1). The precision of the added equivalent of HClO₄ in conjunction with stepwise analysis of the reaction mixture by UV-vis spectroscopy affords the level of control required to manage the equilibrium distribution of species. The approach allows one to carefully optimize the amount of the μ -hydroxo dimer generated, as evidenced by the electronic spectra shown in Figs 7 and 8. (Analogous spectroscopic data are available for the indium and aluminum derivatives in the supporting information, see Figs S2–S4.) Significantly, the DFT-calculated electronic spectra for the postulated reactant, intermediate, and μ -hydroxo dimer product involved in the equilibrium (Fig. 6) afford an acceptable match of the experimentally observed spectra (after appropriate, uniform scaling of the absolute energy values). The calculations clearly confirm the identity of the postulated intermediate, namely the six-coordinate bis(aqua) complex [Ga(OEP)(OH₂)₂]⁺.

Method 1 and *Method 2* (described in the Experimental Section) are two slightly different approaches for the above mentioned synthetic route. We always observe, after following the appropriate synthetic route, a small amount of the starting material, [M(Porph)(OH)], with the crude solid product (*i.e.* the desired μ -hydroxo dimer). For this reason, one or two recrystallizations are required in order to obtain analytically pure dimeric

compounds. The quite different physical characteristics of the starting and product complexes facilitates purification of the desired dinuclear species by recrystallizations from mixtures of dry CH₂Cl₂ and hexanes. No equilibrium between the dinuclear species and their corresponding monomers has been detected in the absence of traces of water or electrolyte salt in the solutions. All efforts to synthesize μ -hydroxo-bridged dinuclear complexes with two different porphyrin macrocycles, *e.g.* {[Ga(OEP)](μ -OH)[Ga(TPP)]}⁺ were unsuccessful. For instance, we found that the *condensation* of a mixture of [Ga(OEP)(OH)] and [Ga(TPP)(OH)] gave rise only to the more thermodynamically favored dimer, namely {[Ga(OEP)]₂(OH)}ClO₄. Furthermore, the monomeric complex with TPP as the porphyrin macrocycle is steadfastly unreactive. In principle, this class of asymmetric dinuclear species would provide an interesting family of complexes in which selective oxidation or reduction of only one of the porphyrin macrocycles might be possible (if the complexes can be made), thereby facilitating the possible formation of mixed-valence complexes.

Electrochemical and DFT data for μ -hydroxo dimers

The electrochemical behavior of {[Ga(OEP)]₂(OH)}ClO₄ and {[Ga(TPP)]₂(OH)}ClO₄ was investigated in CH₂Cl₂ with 0.1 M TBAP as the supporting electrolyte under argon. Two quasireversible waves are observed both in the reduction and oxidation cycles. All electrochemical processes take place in the macrocycle and clearly correspond to a transfer of two electrons.

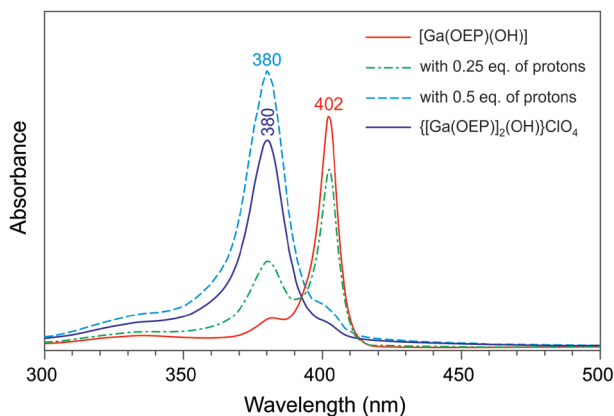


Fig. 7. Electronic spectra monitoring the conversion of monomeric $[\text{Ga}(\text{OEP})(\text{OH})]$ to $\{[\text{Ga}(\text{OEP})_2(\text{OH})]\text{ClO}_4\}$ by treatment with aqueous HClO_4 in CH_2Cl_2 at ambient temperature. The spectrum of the μ -hydroxo complex, $\{[\text{Ga}(\text{OEP})_2(\text{OH})]\text{ClO}_4\}$, was obtained by dissolving clearly identified crystals of the complex. Hence, the absorption scale is not equivalent to that of the other species

Experimentally discrete oxidation or reduction of the individual porphyrin rings of the present group of μ -hydroxo dimers was not observed. This type of behavior has been seen in some, but not all, covalently linked bisporphyrins [22].

Half-wave potentials for oxidation and reduction are given in Table 2 where the redox potentials of their precursors are also included [23]. The absolute potential difference between the first two reduction potentials for $\{[\text{Ga}(\text{TPP})_2(\text{OH})]\text{ClO}_4\}$ is 400 mV while the value for $\{[\text{Ga}(\text{OEP})_2(\text{OH})]\text{ClO}_4\}$ is 450 mV. These separations between the reduction waves are in good agreement with the 420 ± 50 mV generally observed for ring-centered reductions of different metalloporphyrin complexes [23]. The reported range of successive ring-centered oxidations is 240 ± 50 mV [23], consistent with the observed values; this is not the case for the corresponding monomeric species [16].

From our DFT simulations, which are unprecedented for μ -hydroxo metalloporphyrin dimers, it is clear that the HOMO and LUMO of the μ -hydroxo dimers evenly span both porphyrin rings (Fig. 5) and correspond to the typical π -character a_{1u} and e_g frontier MOs of D_{4h} symmetry metalloporphyrins [18–20]. Notably, the Ga(III) ions are located at nodes in these MO wave functions, succinctly accounting for the concerted ring-centered oxidations and reductions observed in the experimental CV scans. The fact that the FMOs (especially the antibonding π^* MOs) do not encompass the μ -hydroxo bridge suggests that the dinuclear species will be redox-stable, consistent with experiment.

The energy of the *gas phase* HOMO and LUMO may be estimated from the experimentally determined first oxidation and first reduction peak potentials of the

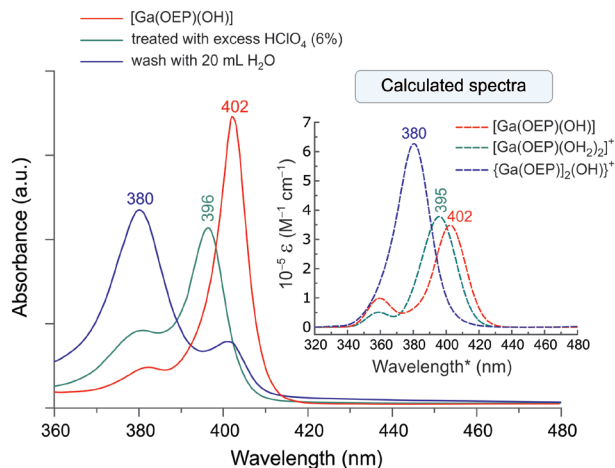


Fig. 8. Electronic spectra recorded in CH_2Cl_2 at ambient temperature illustrating the difference in the Soret band for the starting material $[\text{Ga}(\text{OEP})(\text{OH})]$, the “aqua complex” ($\lambda_{\text{max}} = 396$ nm) and $\{[\text{Ga}(\text{OEP})_2(\text{OH})]\text{ClO}_4\}$ ($\lambda_{\text{max}} = 380$ nm). The DFT-calculated spectra of the relevant species (in a CH_2Cl_2 solvent continuum) are shown in the inset. A correction factor ($\lambda = +25$ nm) was uniformly applied to the calculated energies to match the experimental spectra. The bandwidth for plotting the calculated spectra was 1500 cm^{-1} (FWHM)

system, typically CV measurements conducted in non-aqueous media (*e.g.* CH_3CN with 0.1 M supporting electrolyte and ferrocene, Fc, as the internal reference compound) [24]:

$$E_{\text{HOMO}} = -(E_{[\text{onset, ox vs. Fc}^+/\text{Fc}]} + 5.1 - 0.40) \text{ eV} \quad (2)$$

$$E_{\text{LUMO}} = -(E_{[\text{onset, red vs. Fc}^+/\text{Fc}]} + 5.1 - 0.40) \text{ eV} \quad (3)$$

In these equations, the formal potential of the Fc^+/Fc redox couple (in acetonitrile) is approximately -5.1 eV in the Fermi scale. We've added the $+0.40$ V correction to the equations above to facilitate calculations with redox data measured against SCE (as opposed to the Fc^+/Fc standard redox couple). The experimental peak potentials for the first oxidation and reduction of the Ga(III) complexes listed in Table 2 were used with Eqs. 2 and 3 to calculate the *gas phase* HOMO and LUMO energies of the complexes. The empirical estimates are tabulated with the *in vacuo* DFT-calculated MO energies in Table S4. Although the absolute energies of the HOMO and LUMO exhibit some marked differences between experiment and theory (due to the approximations associated with Eqs. 2 and 3), the most important parameter, ΔE_{FMO} , is notably congruent across this small series of Ga(III) hydroxo derivatives. The maximum deviation between the empirical and DFT-calculated values amounts to $<8\%$ for $[\text{Ga}(\text{OEP})(\text{OH})]$. As far as the μ -hydroxo dimers are concerned, our simulations explain why all reversible electron transfers involve the pair of porphyrin macrocycles equally (*i.e.* no step-wise

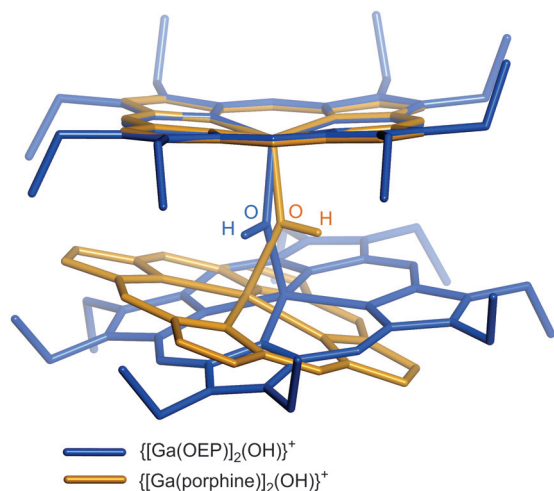


Fig. 9. Molecular overlay (least-squares fit) of the upper Ga(III) porphyrin rings within the μ -hydroxo dimers $\{[Ga(OEP)]_2(OH)\}^+$ and $\{[Ga(porphine)]_2(OH)\}^+$. The figure highlights the effect of the peripheral groups on the overall architecture of the dimer. Most hydrogen atoms have been omitted from the tube model for clarity

electron transfer to separate porphyrin rings is theoretically possible given the nature of the HOMO and LUMO).

The decrease in the magnitude of ΔE_{FMO} upon dimerization of the hydroxo monomer to form the μ -hydroxo dimer (Eq. 1) is largest for the OEP system (0.25 eV, DFT data) and suggests that changing the porphyrin substituents represents one practical method for lowering the energy gap in μ -hydroxo dimers of Ga(III) porphyrins should this be desired for testing the applications of these complexes in OLEDs [25, 26] or solar cells [27]. The decrease in ΔE_{FMO} for $\{[Ga(TPP)]_2(OH)\}^+$ is less significant (0.04 eV) presumably because the π - π interaction between the porphyrin rings is sterically limited by the bulky *meso*-phenyl groups. While repulsive steric interactions between substituent groups appended to the porphyrin rings undoubtedly affect the ring-ring separation, this is not the only geometrical change mediated by intramolecular peripheral group steric effects. Thus, the Ga-O bond distances, Ga-O-Ga bond angle, and N-M-M-N twist angle governing the relative orientations of the rings within the dimer also change, as evidenced by the superimposed gas phase structures of $\{[Ga(OEP)]_2(OH)\}^+$ and $[Ga(porphine)]_2(OH)^+$ shown in Fig. 9. All of these factors in unison with the π - π interaction and electronic character of the porphyrin substituents (*e.g.* inductively electron-releasing ethyl groups) are likely to modulate the FMO energy gap in the dimer and thus the net change in the gap relative to the monomer.

NMR spectroscopy

1H NMR spectroscopy. The formation of the μ -hydroxo bridge upon condensation of $[M(Porph)]$

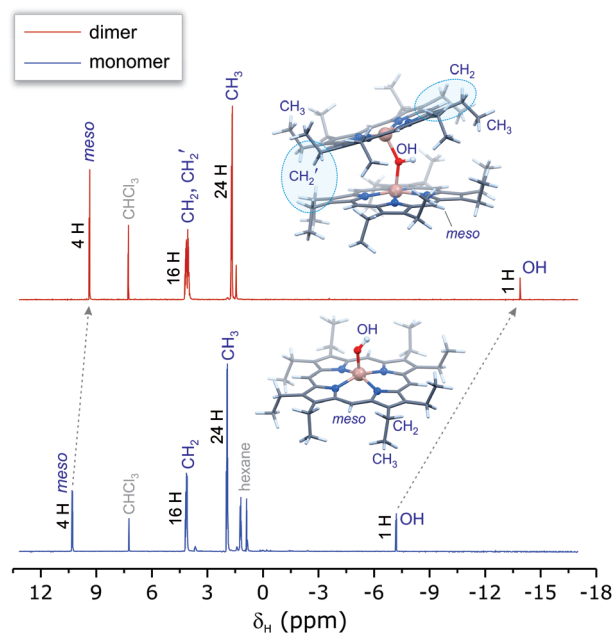


Fig. 10. Ambient temperature 1H NMR spectra for $[Ga(OEP)(OH)]$ and $\{[Ga(OEP)]_2(OH)\}ClO_4$ recorded in $CDCl_3$. Signal assignments are indicated along with integral ratios. The DFT-calculated structure of the μ -hydroxo dimer highlights the two inequivalent magnetic environments for the methylene protons of the ethyl groups

(OH)] causes an upfield shift of all proton signals for both dimers (OEP and TPP) relative to their monomeric precursors. For $[Ga(OEP)(OH)]$ and $\{[Ga(OEP)]_2(OH)\}ClO_4$, the signal from the *meso* protons is shifted upfield to 9.36 ppm in the dimer from 10.30 ppm in the monomer (Fig. 10). The signal from the pyrrole β -protons of the TPP complex exhibits an upfield shift of 0.4 ppm. Similar changes in the chemical shifts of the *meso* and pyrrole β proton signals have also been observed for the (OEP)Rh-In(OEP) and (OEP)Rh-Tl(OEP) complexes [16]. This upfield shift in δ_H can be attributed to significant aromatic ring current induced shielding [28] in the *intra* dimer region between porphyrin rings that are in close proximity.

In μ -hydroxo dimers, a further consequence of two porphyrin ring currents intersecting in the *intra* dimer space is that any *peripheral group* protons located in the region between the two macrocycles (*i.e.* the outer reaches of the *endo* region depicted in Fig. 2) are effectively “doubly deshielded”, while protons outside that region positioned toward the solvent (the *exo* region depicted in Fig. 2), are only “singly deshielded” due to the operation of a single conical shielding cone and peripheral deshielding zone on the solvent-exposed outer face of each porphyrin macrocycle of the dimer. The net effect is that peripheral group *exo* protons in Group 13 μ -hydroxo metalloporphyrin dimers are *relatively shielded* compared with their chemically-equivalent counterparts located within the *endo* region of the complex. The magnetic anisotropy

is especially pronounced in $\{[\text{Ga}(\text{TPP})_2(\text{OH})]\text{ClO}_4\}$, as summarized in Table 1, and accounts for the chemical shift difference of 0.41 ppm between the *o-endo* and *o-exo* protons of the *meso*-phenyl groups.

In the case of $\{[\text{Ga}(\text{OEP})_2(\text{OH})]\text{ClO}_4\}$, the ring current-induced magnetic anisotropy in the slow exchange limit accounts for the split signal and chemical shift inequivalence of the β -methylene (CH_2) protons of the ethyl groups appended to the porphyrin rings (Table 1, Fig. 10). Magnetic anisotropy for the β - CH_2 protons of $[\text{Ga}(\text{OEP})(\text{OH})]$ was, however, not observed at ambient temperature, despite the 5-coordinate geometry of the monomeric complex, due to free rotation of the ethyl groups and thus signal averaging (as evidenced by the ^{13}C spin-lattice relaxation rates in Table S2, *vide infra*). This behavior contrasts that of $[\text{Ga}(\text{TPP})(\text{OH})]$ which has magnetically inequivalent *o*-phenyl protons in the slow exchange limit due to asymmetry (structurally distinct faces of the macrocycle engendered by the single hydroxo ligand) and a significant barrier to free rotation of the *meso*-phenyl rings [29] (*vide infra*). Our observations for $\{[\text{Ga}(\text{OEP})_2(\text{OH})]\text{ClO}_4\}$ regarding the anisochronous β -methylene protons are consistent with other studies on monomeric metalloporphyrins containing Tl(III) [30–32], five-coordinate $[\text{Ga}(\text{OEP})\text{X}]$ derivatives (where X = halogen) [33], and $[\text{Sc}(\text{OEP})_2(\text{O})]$ (a structurally-related μ -oxo-dimer) [34].

Regarding the DFT-calculated isotropic shieldings, the calculated ^1H chemical shifts are in good agreement with the experimental chemical shifts. The smallest deviations (< 0.4 ppm) are for the porphyrin β - and *meso*-protons as well as the ethyl group protons of $[\text{Ga}(\text{OEP})_2(\text{OH})]^+$. The chemical shift pattern and relative shielding for the *endo* and *exo ortho*-phenyl ring protons of $\{[\text{Ga}(\text{TPP})_2(\text{OH})]^+\}$ is similarly well modeled, the deviation between experiment and theory amounting to < 0.8 ppm. A similar level of agreement holds for the *para* and *meta* protons. As noted above, the hydroxo group protons of the five-coordinate monomers, $[\text{Ga}(\text{Porph})(\text{OH})]$, are shielded by virtue of their location within the ring current shielding zone above the porphyrin macrocycle. The calculated isotropic shieldings for the monomer OH protons (-5.4 to -6.1 ppm, Table 3) are in broad agreement with the experimental chemical shifts (-6.6 to -7.2 ppm) and correlate with the charge on the H atom and ΔE_{FMO} (Fig. S8). Importantly, the enhanced shielding brought about by μ -hydroxo dimer formation and sandwiching of the OH proton between the bridged porphyrin rings is confirmed by the DFT simulations, which predict a strong upfield shift in the δ_{H} values to -12.0 to -12.9 ppm. (The experimental chemical shifts are -13.9 and -14.5 ppm for the TPP and OEP dimers, respectively).

^{13}C NMR spectroscopy. The ^{13}C chemical shifts for both μ -hydroxo Ga(III) porphyrin dimers are summarized in Table S1. For the TPP complex, the phenyl carbons are, similar to the phenyl protons, magnetically inequivalent (Table 1). However, the *meta* carbons in the

endo region (*m-endo*) resonate at a slightly higher magnetic field relative to the *meta* carbons in the *exo* region (*m-exo*). In the ^1H NMR spectrum by contrast, both the *ortho* and *meta* protons in the *exo* region resonate at a higher magnetic field relative to the corresponding protons in the *endo* region.

^{13}C spin-lattice relaxation data in Table S2 (measured at $B_0 = 11.74$ T) are presented as NT_1 , where N is the number of protons directly attached to an individual carbon atom. Listing the data as NT_1 accounts for the different numbers of protons present in methine (CH), methylene (CH_2), and methyl (CH_3) groups, and enables one to directly compare the dynamics of various molecular segments within the μ -hydroxo dimers. For $\{[\text{Ga}(\text{TPP})_2(\text{OH})]\text{ClO}_4\}$, the NT_1 values for the pyrrole β -carbons are, within experimental error, equal to the NT_1 values of the phenyl *para* carbons. The NT_1 values of the *ortho* and *meta* carbons of the phenyl rings are similarly equivalent within experimental error. However, they are higher than those of both the pyrrole β -carbons and the *meso*-phenyl *para*-carbons. This fact demonstrates that the phenyl rings of the TPP dimer undergo dynamic internal reorientation (rotation) about their two-fold symmetry axes.

The relaxation rates of the methylene and methyl carbon nuclei of $\{[\text{Ga}(\text{OEP})_2(\text{OH})]\text{ClO}_4\}$ are higher than the rate observed for the TPP *meso*-phenyl carbons, consistent with the overall higher internal mobility of the sterically less bulky peripheral ethyl groups in the OEP dimer.

We have analyzed ^{13}C NMR relaxation data of carbon atoms with directly attached protons for $\{[\text{Ga}(\text{TPP})_2(\text{OH})]\text{ClO}_4\}$ assuming direct ^{13}C - ^1H dipolar interactions to be the dominant relaxation mechanism. Using NMR relaxation theory [35, 36], the spin-lattice relaxation rates $R_1 = (NT_1)^{-1}$ and NOE factors can be expressed as a combination of spectral densities of motion $J_i(\omega_j)$ in the following manner [37],

$$R_1 = \frac{1}{20} \left(\frac{\gamma_{\text{H}} \gamma_{\text{C}} \hbar}{2\pi r_{\text{CH}}^3} \right)^2 \left\{ J_0(\omega_{\text{H}} - \omega_{\text{C}}) + 3J_1(\omega_{\text{C}}) + 6J_2(\omega_{\text{H}} + \omega_{\text{C}}) \right\} \quad (4)$$

$$\text{NOE} = 1 + (\gamma_{\text{H}}/\gamma_{\text{C}}) \frac{\{6J_2(\omega_{\text{H}} + \omega_{\text{C}}) - J_0(\omega_{\text{H}} - \omega_{\text{C}})\}}{\{J_0(\omega_{\text{H}} - \omega_{\text{C}}) + 3J_1(\omega_{\text{C}}) + 6J_2(\omega_{\text{H}} + \omega_{\text{C}})\}} \quad (5)$$

where γ_{H} and γ_{C} are the magnetogyric ratios of the ^1H and ^{13}C nuclei, respectively, \hbar is Planck's constant and r_{CH} is the C-H bond length. ω_{H} and ω_{C} are the Larmor frequencies for ^1H and ^{13}C , respectively. The spectral densities of motion, $J_i(\omega_j)$ ($i = 0, 1, 2$; $\omega_j = \omega_{\text{H}} - \omega_{\text{C}}$, ω_{C} , $\omega_{\text{H}} + \omega_{\text{C}}$), are Fourier transforms of the corresponding correlation functions $G_i(\tau)$. The correlation functions $G_i(\tau)$ describe fluctuations in the ^{13}C -H bond orientation with respect

to the static magnetic field B_0 in terms of the second rank tensor components which characterize the dipolar coupling [35].

In order to analyze the experimental R_1 and NOE data, the correlation functions $G_i(\tau)$ must be derived from a specific physical model describing fluctuations of the dipolar coupling associated with a given ^{13}C - ^1H bond. Based on the crystal structure of $\{[\text{Mn}(\text{TPP})_2(\text{OH})]\text{ClO}_4$ [12] we have employed a simple model of overall (isotropic) molecular tumbling for the phenyl *para*- and pyrrole β -carbons, and a model of composite motion consisting of overall molecular tumbling and a jump motion about the two-fold symmetry axis of the phenyl ring between two equally populated positions (rotamers) for the *ortho* and *meta* carbons. Calculation of the correlation functions leads to the spectral densities of the form [37]

$$J_i(\omega_j) = 2[\tau_{\text{iso}} / (1 + \omega_j^2 \tau_{\text{iso}}^2)] \quad (6)$$

for the isotropic reorientation and

$$J_i(\omega_j) = 2 \left\{ (1 - C) \left[\frac{\tau_{\text{iso}}}{(1 + \omega_j^2 \tau_{\text{iso}}^2)} \right] + C \frac{(\tau_{\text{iso}}^{-1} + \tau_{\text{jump}}^{-1})^{-1}}{1 + \omega_j^2 (\tau_{\text{iso}}^{-1} + \tau_{\text{jump}}^{-1})^{-2}} \right\} \quad (7)$$

for the composite motion, where

$$C = 3/4[\sin 2\beta(1 - \cos 2\theta)][2 - \sin 2\beta(1 - \cos 2\theta)] \quad (8)$$

and τ_{iso} and τ_{jump} are the correlation times corresponding to the isotropic reorientation and the jump about the two-fold symmetry axis of the phenyl ring, respectively. β is the angle between the relaxation vector (^{13}C - ^1H bond) and the axis about which the vector jumps, while the angle 2θ is the extent of the jump.

The results of the analysis of the experimental T_1 and NOE data in terms of the motional models (Eqs. 1–5, *vide supra*) are presented in Tables S2 and S3. The model of isotropic reorientation fits the experimental data for the pyrrole β carbon nuclei and the phenyl *para* carbons at all temperatures, with the exception of the NOE at 20 °C. In this case, the calculated NOE value is outside (above) the error range of the experimental NOE. The calculated T_1 values for the *meso*-phenyl ring *ortho* and *meta* carbons using the model of composite motion for these nuclei are consistent with those measured experimentally, further validating the model.

^{71}Ga NMR spectroscopy. Gallium possesses two stable isotopes, ^{69}Ga and ^{71}Ga , that have a nuclear spin $I = 3/2$ and a quadrupole moment [35]. As ^{71}Ga has higher receptivity and provides sharper resonance lines than ^{69}Ga , we have measured the NMR spectra of the former isotope. The chemical shift range of the ^{71}Ga nucleus is

~1400 ppm. This is due to a dominance of the paramagnetic term in the nuclear screening constant. The ^{71}Ga NMR resonance signals of the monomeric precursors of both dimers are at a lower magnetic field relative to the reference signal from $\text{Ga}(\text{NO}_3)_3$. The chemical shifts for $[\text{Ga}(\text{OEP})(\text{OH})]$ and $[\text{Ga}(\text{TPP})(\text{OH})]$ measured 72.8 and 77.1 ppm, respectively. These δ_{Ga} values are significantly shielded relative to the chemical shifts ($\delta_{\text{Ga}} \sim 110$ – 171 ppm) observed for aliphatic triazamacrocyclic chelates of the metal ion, which are of considerable interest as potential biomedical imaging agents [38, 39]. Interestingly, the octahedral $\text{Ga}(\text{III})$ complex $[\text{Ga}(\text{H}_3\text{ppma})_2][\text{NO}_3]_3$ [40], where $\text{H}_3\text{ppma} = \text{tris}(4\text{-}(\text{phenylphosphinato})\text{-3-methyl-3-azabutyl})\text{amine}$, has 6 neutral oxygen donor atoms and exhibits a significantly more shielded ^{71}Ga NMR chemical shift (-62.3 ppm) relative to the $[\text{Ga}(\text{Porph})(\text{OH})]$ derivatives.

No observable signal was detected for the corresponding μ -hydroxo dimers despite scanning a wide region of the ^{71}Ga NMR chemical shift range (-1000 ppm to $+1000$ ppm around the reference signal). The signal is most likely very broad due to the interaction of the quadrupole moment of ^{71}Ga with the electric field gradient created by the negative charge localized on the oxygen atom of the hydroxo bridge (Table 3), and thus undetectable with a high-resolution NMR spectrometer. (High-resolution instruments generally have limited hardware capabilities to measure broad resonance signals of ~ 100 KHz.)

X-ray crystallography

The structures of the Group 13 μ -hydroxo metalloporphyrin dimers elucidated here are broadly similar to the μ -hydroxo-bridged species of other $\text{M}(\text{III})$ porphyrins determined previously [9, 11, 12]. Side-on views of the X-ray structures of $\{[\text{Ga}(\text{OEP})_2\text{OH}^+]\}$ and $\{[\text{In}(\text{OEP})_2\text{OH}^+]\}$ depicted in Figs 3 and 4 (for the triclinic polymorph of the indium derivative) indicate the structural features to be considered, namely the $\text{M}-\text{N}_p$ and $\text{M}-\text{O}(\text{OH})$ bond distances, the $\text{M}-\text{O}(\text{OH})-\text{M}$ bond angle, and the dihedral angle between the two porphyrin rings (among others).

The $\text{M}-\text{O}(\text{OH})-\text{M}$ bond angles differ substantially from the ideal value of $\sim 104.48^\circ$ for an sp^3 -hybridized oxygen atom in water [41] and reflect both the bonding requirements of the central metal ion, including the $\text{M}-\text{O}(\text{OH})$ bond length, and the steric requirements of the porphyrin ligand. These views also show an unusual feature found in all three unique indium μ -hydroxo species, namely that the hydrogen atom of the bridging OH ligand is hydrogen-bonded to a solvate water molecule with normal hydrogen bonding distances. The appearance of these hydrogen bonds may reflect reduced basicity of the OH bridging group in the indium derivatives, a postulate that is consistent with the more positive H and less negative O atom charges calculated for the μ -hydroxo dimers relative to the $[\text{Ga}(\text{Porph})(\text{OH})]$

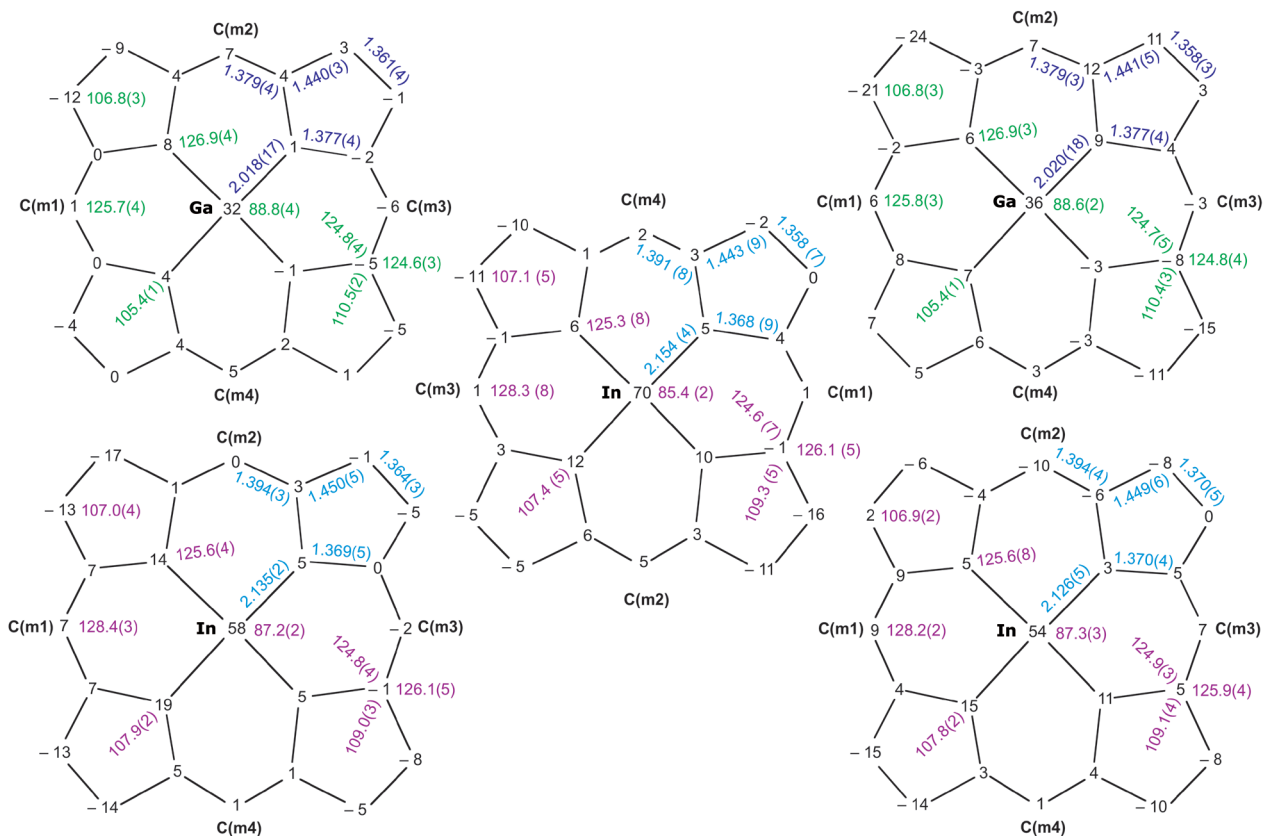


Fig. 11. Mean plane diagrams for the two rings of $\{[\text{Ga}(\text{OEP})_2(\text{OH})]^+\}$ (top line), monomeric $[\text{In}(\text{OEP})(\text{OH})]$ (center), and the two rings of the monoclinic polymorph of $\{[\text{In}(\text{OEP})_2(\text{OH})]^+\}$ (bottom line). Displayed on each diagram are the displacements of each atom (in units of 0.01 \AA) from its respective 24-atom mean plane. Also shown are the averaged values (4-fold symmetry) of the bond distances and bond angles in the core. The numbers in parentheses are the estimated standard uncertainties based on the assumption that all values are drawn from the same population

monomers (Table 3). Also revealed in these two figures is that the hydrogen atom of the OH group in three of the four dinuclear complexes was experimentally located (difference Fourier synthesis). The values of the coordination group in the reported complexes along with previously reported species are given in Table 4.

Table 4 shows that the $\text{M}\cdots\text{M}$ separations display much smaller variation than other quantitative descriptors, reflecting the importance of repulsion between the porphyrin ligands in determining the overall stereochemistry of the μ -hydroxo dimers. The porphyrin–porphyrin interactions also favor “outward” orientations of the peripheral ethyl groups (*i.e.* most of the ethyl groups are oriented away from the molecular center with an *exo*-configuration). These interactions may also affect the $\text{N}-\text{M}-\text{N}$ twist angles (Table 4). Diagrams illustrating the overlap between the rings are given in Fig. 12.

The values of the $\text{M}-\text{N}_p$ and $\text{M}-\text{O}(\text{OH})$ bond distances are in general accord with values typical of the respective metal of the dinuclear species. Additional stereochemical parameters include the ring size, which is given by the average ring center (Ct) to N_p distance. The

values for the Fe, Mn, and Ga derivatives reflect values for the porphyrin rings with least strain. The much larger values for the indium derivatives ($\sim 2.08 \text{ \AA}$) reflect the larger size of the indium(III) ion, as do the values of the $\text{In}-\text{N}_p$ bond distances. The large size of the indium ion is also reflected in the increased displacement of the metal ion from both the mean plane of the 24-atom core and the plane of the 4N core. The difference in these two values, especially pronounced for the indium species, also reveals that substantial doming of the porphyrin macrocycle occurs, which is another stereochemical feature to accommodate larger metal ions [43, 44]. Moreover, the differences in the value of the dihedral angles between the 24-atom mean planes and four nitrogen atom mean planes indicate that distortions from planarity accommodate the close approach of the porphyrin rings.

Regarding the metalloporphyrin conformations for this group of structurally-related derivatives, Fig. 11 displays the perpendicular displacements of the ring atoms from the 24-atom mean plane of the porphyrin core. The diagram also presents the average values of bond distances and bond angles in the core. The differences

Table 4. Comprehensive list of crystallographically-determined structural parameters for metalloporphyrin μ -hydroxo dimers

	{[Mn(OEP)] ₂ - (OH)}ClO ₄	{[Mn(TPP)] ₂ - (OH)}ClO ₄	{[Fe(OEP)] ₂ - (OH)}ClO ₄	{[Ga(OEP)] ₂ - (OH)}ClO ₄	{[In(OEP)] ₂ - (OH)}ClO ₄ ^a	{[In(OEP)] ₂ - (OH)}ClO ₄ ^b	{[Ga(OEP)] ₂ - (OH)}ClO ₄	{[In(OEP)] ₂ - (OH)}TFPB ^k
M...M ^c	3.909	3.993	3.707	3.677	3.927	3.966	— ^d	— ^d
M(1)-O ^c	1.998 (2)	2.025 (23)	1.924 (2)	1.911 (2)	2.081 (3)	2.101 (3)	1.9953	2.119 (1)
							2.213 (3) ^e	
M(2)-O ^c	2.024 (2)	2.028 (18)	1.952 (2)	1.911 (2)	2.090 (3)	2.090 (3)	1.895 (3)	2.119 (1) ^f
M(1)-N ^c _p	2.006 (6)	2.008 (7)	2.036 (13)	2.018 (17)	2.136 (4)	2.135 (2)	2.029 (9)	2.136 (6)
M(2)-N ^c _p	2.007 (6)	2.008 (8)	2.039 (8)	2.020 (18)	2.133 (4)	2.126 (5)	2.036 (6)	2.136 (6) ^f
Cr(1)...N ^c _p	1.993 (2)	1.998 (5)	2.001 (1)	1.997 (12)	2.080 (2)	2.082 (3)	— ^d	— ^d
Cr(2)...N ^c _p	1.996 (5)	1.995 (6)	2.002 (4)	1.996 (20)	2.082 (4)	2.076 (2)	— ^d	— ^d
M-O(H)-M	152.7 (1)	160.4 (8)	146.2 (2)	148.3 (1)	140.6 (2)	142.3 (1)	152.0 (2)	144.5 (2)
O-M(1)-N (avg) ^g	96.4 (2.3)	96.0 (6.1)	100.6 (1.9)	98.2 (5.3)	103.0 (4.6)	102.8 (6.6)	92 (4)	100 (5)
O-M(2)-N (avg) ^g	95.9 (8.4)	96.3 (5.6)	100.8 (10.3)	98.9 (5.4)	102.6 (2.6)	102.5 (2.6)	100 (5)	106 (5)
N-M-M'-N' (avg) ^g	4.3 (0.8)	29.9 (0.6)	8.4 (1.8)	13.4 (0.5)	18 (3)	13 (3)	22	23
$\Delta M(1)24^{e,h}$	0.23	0.19	0.41	0.32	0.58	0.58	— ^d	— ^d
$\Delta M(2)24^{e,h}$	0.19	0.20	0.44	0.36	0.58	0.54	— ^d	— ^d
$\Delta M(1)N4^{e,i}$	0.22	0.21	0.37	0.29	0.48	0.48	— ^d	— ^d
$\Delta M(2)N4^{e,i}$	0.21	0.22	0.39	0.31	0.46	0.46	— ^d	— ^d
24MP DA ^{g,j}	12.69	3.96	19.92 ^d	16.4	31.06	26.13	15.0	23.0
N4MP DA ^{g,j}	15.48	6.35	22.84	19.0	33.74	29.35	— ^d	— ^d
Ref.	9	11	12	tw	tw	tw	15	15

^aTriclinic form. ^bMonoclinic form. ^cValue in Å. ^dNot reported. ^eSixth ligand. ^fRequired by symmetry. ^gValue in degrees. ^hMetal displacement from 24-atom mean plane. ⁱMetal displacement from porphyrin nitrogen atom mean plane (N4). ^jDihedral angle. ^kTFPB = 4,4,4-trifluoro-1,3-dioxo-1-phenylbutan-2-ide.

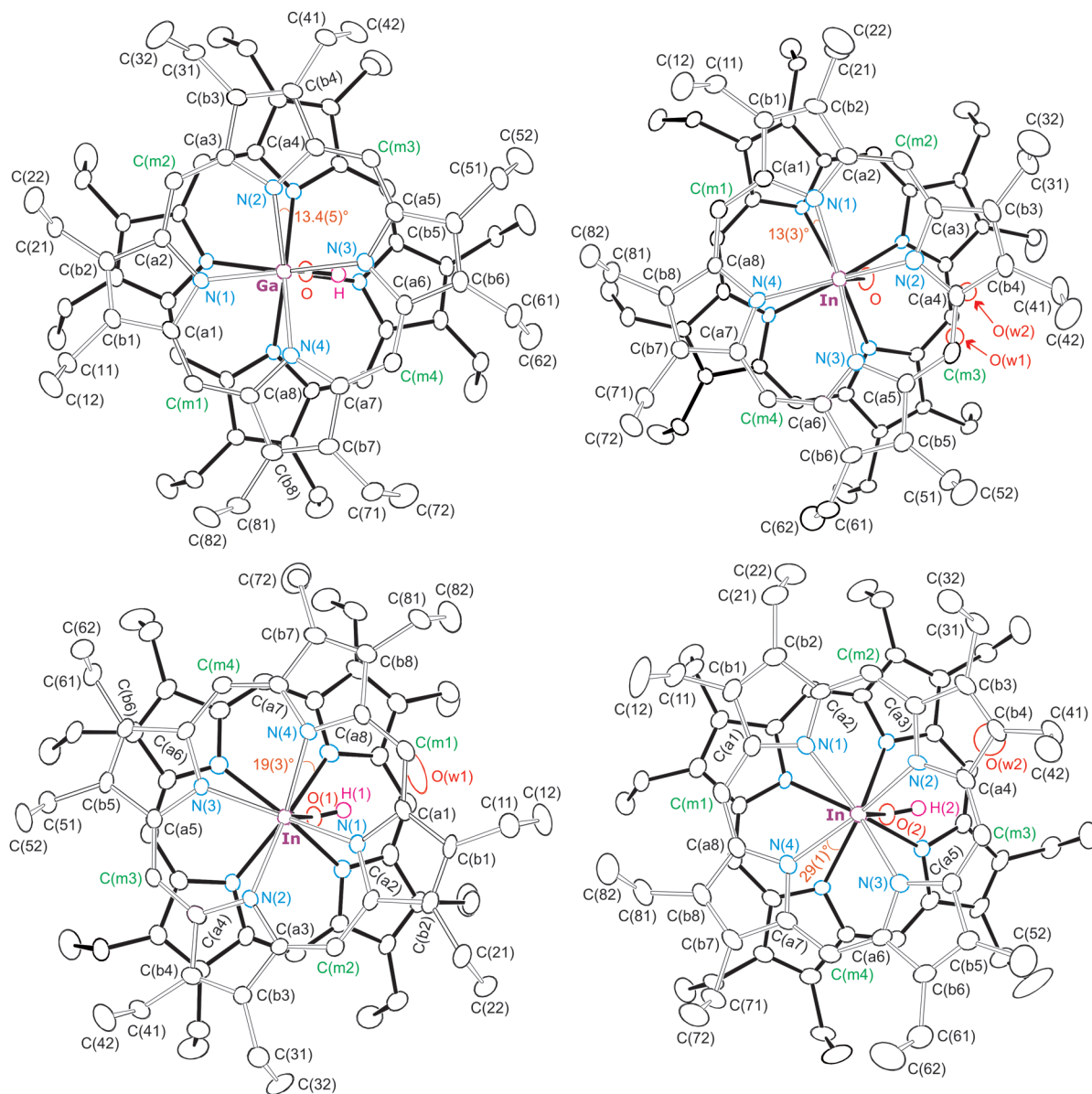


Fig. 12. Thermal ellipsoid diagrams illustrating the overlap between the two porphyrin rings in each of the four dinuclear species reported here. All atoms are contoured at the 50% probability level. In all diagrams, the top ring is shown with unshaded bonds. Top left: $\{[\text{Ga}(\text{OEP})]_2(\text{OH})\}\text{ClO}_4$, Top right: $\{[\text{In}(\text{OEP})]_2(\text{OH})\}\text{ClO}_4$, Bottom left: $\{[\text{In}(\text{OEP})]_2(\text{OH})\}\text{ClO}_4$ (molecule 1, triclinic phase), Bottom right: $\{[\text{In}(\text{OEP})]_2(\text{OH})\}\text{ClO}_4$ (molecule 2, triclinic phase). All H atoms except those located on the bridging oxygen atom (when located) have been omitted for clarity; the perchlorate counterions are also not shown.

in the core metrical parameters between those of the gallium species (top line) and those of the indium species (bottom line) are the result of the core expansion accommodating metal ions of substantially different sizes. In the gallium/indium comparison, the $\text{C}_a\text{-C}_m\text{-C}_a$ bond angle opens up by $\sim 3^\circ$ in the indium species along with an increase of $\sim 2.5^\circ$ in the $\text{C}_a\text{-N-C}_a$ bond angle. An increase in the bond length of the $\text{C}_a\text{-C}_m$ bonds also contributes to increasing the size of the porphyrin ring. Similar patterns are seen in the remaining indium derivatives that are reported in Fig. S5 of the Supporting Information.

Although solution state evidence (^1H NMR and electronic spectroscopy) confirms the formation of monomeric hydroxide complexes of all Group 13 species, we have only obtained crystals of $[\text{In}(\text{OEP})(\text{OH})]$. The five-coordinate species is illustrated in Fig. S6 (Supporting Information). The complex forms an extended structure with weak $\pi\text{-}\pi$ interactions between porphyrin rings (Fig. 13). For the centrosymmetric inversion pair, the $\text{In}\cdots\text{In}$ distance measures 8.60 \AA , while the interplanar spacing is close to the graphite spacing of 3.44 \AA [42]. These metrics are consistent with a weak edge-to-edge type $\pi\text{-}\pi$ interaction, as reviewed earlier by Scheidt and Lee [43].

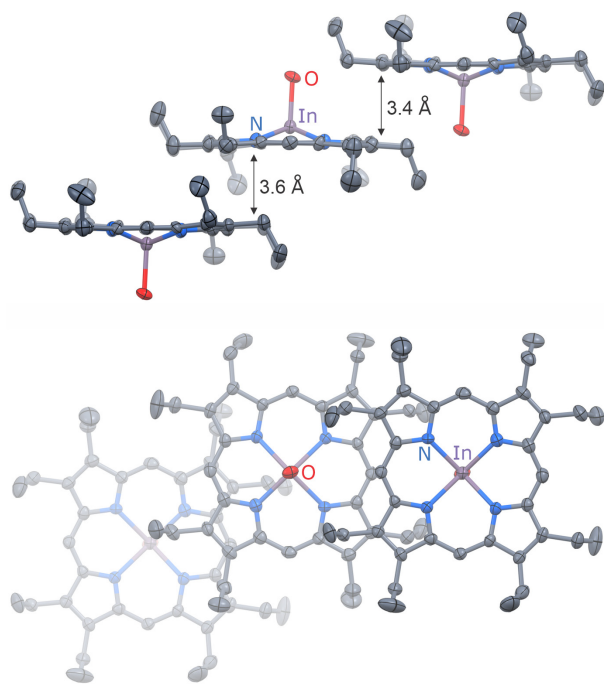


Fig. 13. Two views highlighting the distinct edge-to-edge π - π interactions between molecules of five-coordinate [In(OEP)(OH)]. Key interplanar spacings (based on the distance between parallel 24-atom porphyrin mean planes) are depicted for the edge-on view (top), while the lower image (perpendicular view) highlights the relationship between the inversion pair and the closest adjacent molecule (right most structure) in the lattice. H atoms have been omitted for clarity; thermal ellipsoids are rendered as 40% probability surfaces. Darkly shaded objects are closest to the viewer.

EXPERIMENTAL SECTION

General methods

H₂OEP was purchased from Midcentury Chemicals and H₂TPP was prepared according to the literature [45]. Dichloromethane, hexane, glacial acetic acid, sodium acetate, and alumina adsorbent (80–200 mesh) were bought from Fisher; perchloric acid (~70%), gallium chloride, indium chloride, and aluminum chloride were purchased from Aldrich. All materials were used as received unless otherwise noted. Dichloromethane for electrochemical studies was distilled over CaH₂ and subsequently over P₂O₅. Tetrabutylammonium perchlorate, TBAP, was purchased from GFS Chemicals and was always stored in a vacuum oven at +40.0 °C. Aqueous perchloric acid was prepared by diluting the original concentrated acid 1000-fold prior to determining its exact concentration by standard acid-base titrations against potassium acid phthalate. IR spectra were recorded on a Perkin-Elmer 883 Infrared Spectrophotometer as Nujol mulls with CsBr disks; electronic spectra were recorded on a Perkin Elmer Lambda 19 UV/vis/near-IR Spectrometer. *Caution!*

Although we have experienced no problem with the procedures described in dealing with systems containing perchlorate ion, they can detonate spontaneously and should be handled only in small quantities; in no case should such a system be heated above 30 °C and other safety precautions are also warranted [46].

Compound synthesis

Synthesis of [Al(OEP)Cl]. [Al(OEP)Cl] was synthesized by metallation of H₂(OEP) with anhydrous AlCl₃ in refluxing benzonitrile according to the literature method [47]. IR (cm⁻¹): 440(s) ($\nu_{\text{Al-Cl}}$).

Synthesis of [Ga(OEP)Cl] and [In(OEP)Cl]. The procedure used to prepare [Ga(OEP)Cl] and [In(OEP)Cl] was essentially that of Bhatti *et al.* [48]. H₂OEP (500 mg) and GaCl₃ (InCl₃) (1.0 g) were added to a hot solution of glacial acetic acid (300 mL) containing 5 g of sodium acetate. The solutions were then refluxed for about 3 h until the UV/vis spectra showed the disappearance of the characteristic bands of octaethylporphyrin free base. The solutions were cooled down to room temperature and then to lower temperatures with an ice-water bath. Crystalline [Ga(OEP)Cl] or [In(OEP)Cl] were obtained by vacuum filtration of the cooled solutions and washed with hexane. IR cm⁻¹: ($\nu_{\text{M-Cl}}$) 333(s) ([Ga(OEP)Cl]) and 308(s) ([In(OEP)Cl]).

Syntheses of [M(OEP)(OH)], M = Al, Ga and In. A slightly modified literature method for [Al(OEP)(OH)] [23] was employed to synthesize [Al(OEP)(OH)], [Ga(OEP)(OH)] and [In(OEP)(OH)]. In a typical preparation, crystalline [Ga(OEP)Cl] or [In(OEP)Cl] (~200 mg) were dissolved in ~50 mL of CH₂Cl₂ and chromatographed on alumina (80–200 mesh) column. Elution with CH₂Cl₂ removed a small amount of free base; the metalloporphyrin complexes were washed out from the column by a mixture of CH₂Cl₂ and methanol (4:1 v:v), and taken to dryness under vacuum. Spectroscopic data for [Al(OEP)(OH)]: IR (cm⁻¹): ($\nu_{\text{O-H}}$) 3655 (w). UV/vis (nm, CH₂Cl₂): λ_{max} 332, 377, 397 (Soret), 531, 570. [Ga(OEP)(OH)]: IR (cm⁻¹): ($\nu_{\text{O-H}}$) 3663 (w). UV/vis (nm, CH₂Cl₂): λ_{max} 336, 382, 402 (Soret), 534, 571. [In(OEP)(OH)]: IR (cm⁻¹): ($\nu_{\text{O-H}}$) 3658 (w). UV/vis (nm, CH₂Cl₂): λ_{max} 344, 388, 408 (Soret), 540, 577.

The indium derivative synthesized above was recrystallized by diffusion of hexane into a toluene solution of the complex. A single-crystal X-ray analysis confirmed that the product complex was [In(OEP)(OH)]. Moreover, an IR spectrum for the single crystal sample displayed an identical O–H stretch (at 3658 cm⁻¹) as that for the powder sample.

Synthesis of [Ga(TPP)(OH)]. To H₂TPP (231 mg, 0.376 mmol) and sodium acetate (5 g) was added a solution of GaCl₃ (525 mg, 2.98 mmol) in 250 mL of glacial acetic acid. The resulting dark green solution was refluxed under argon for 4 h until deep purple in color. TLC on silica gel (1:1 ether:benzene) indicated about

95% conversion of H_2TPP ($R_f = 0.64$) to $[Ga(TPP)Cl]$ ($R_f = 0.46$). 250 mL of distilled water was added to the cooled solution and the metalloporphyrin extracted into 250 mL of toluene in a separatory funnel. The toluene extract was washed twice with distilled water (200 mL), dried over anhydrous calcium chloride, filtered, and taken to dryness on a rotary evaporator. $[Ga(TPP)Cl]$ was converted to the hydroxide derivative by anion exchange on an aluminum oxide column (17.8×3.8 cm, CH_2Cl_2) as described above. The pink–purple solution of $[Ga(TPP)(OH)]$ was then concentrated by rotary evaporation to yield a purple microcrystalline product. Spectroscopic data for $[Ga(TPP)(OH)]$: IR (cm^{-1}): 3664 (w) (ν_{O-H}), 444 (w) (ν_{Ga-O}). UV/vis (nm, CH_2Cl_2): λ_{max} 275, 314, 399 (N), 419.5 (Soret), 550, and 590.

Synthesis of $\{[Ga(OEP)]_2(OH)\}ClO_4$. *Method 1:* In a separatory funnel, a CH_2Cl_2 solution (~20 mL) of $[Ga(OEP)(OH)]$ (~50 mg) was treated with various amounts of aqueous $HClO_4$ ($C = 1.36 \times 10^{-2}$ M). When approximately one-half of an equivalent of acid was used, the Soret band at 402 nm gradually diminished to a shoulder and a new Soret band at 380 nm appeared. The CH_2Cl_2 phase was separated, dried with solid Na_2SO_4 and then taken to dryness under vacuum. The powder material so obtained was recrystallized from CH_2Cl_2 and hexane. After about five days single crystals were isolated. An X-ray structure determination identified the crystal form of the complex as $\{[Ga(OEP)]_2(OH)\}ClO_4$. UV/vis (nm, CH_2Cl_2) for the single-crystal sample of $\{[Ga(OEP)]_2(OH)\}ClO_4$: λ_{max} 335 (sh), 380 (Soret), 400 (sh), 539, 572, and 585 (sh).

Method 2: If the initial CH_2Cl_2 solution of $[Ga(OEP)(OH)]$ was treated with excess aqueous $HClO_4$ (50 mL, 6% v/v), a Soret band was observed at 396 nm. After separation, the CH_2Cl_2 phase was washed with 20 mL of distilled water. The UV/vis spectrum displayed a blue shift of the Soret band to 380 nm. Single crystals were obtained with the same procedure described above. These crystals show identical electronic spectra to the material prepared by *Method 1*. A single crystal unit cell determination by X-ray diffraction also confirmed that the product had the same cell parameters as that prepared by *Method 1*.

Synthesis of $\{[In(OEP)]_2(OH)\}ClO_4$. The identical procedures of *Method 1* and *Method 2* for $\{[Ga(OEP)]_2(OH)\}ClO_4$ were applied for the synthesis of $\{[In(OEP)]_2(OH)\}ClO_4$, starting from $[In(OEP)(OH)]$. With *Method 1*, the blue-shift of the Soret band maximum from 408 nm ($[In(OEP)](OH)$) to 388 nm was observed. Crystallization of the product from a toluene solution of the product layered with hexane yielded crystals with a Soret band maximum at 388 nm only. An X-ray structure analysis identified the compound as $\{[In(OEP)]_2(OH)\}ClO_4$ (triclinic form). With *Method 2*, the blue-shift of the Soret band from 406 nm (aqua/perchlorato complex) to 388 nm was observed. Crystallization from a toluene solution of the product layered with hexane also gave crystals

with a Soret band maximum at 388 nm only. An X-ray analysis identified the compound as $\{[In(OEP)]_2(OH)\}ClO_4$ in a different crystal form (monoclinic polymorph). UV/vis (nm, CH_2Cl_2) for the single crystal sample of $\{[In(OEP)]_2(OH)\}ClO_4$: λ_{max} 345 (sh), 388 (Soret), 407 (sh), 542, 580.

Synthesis of $\{[Ga(TPP)]_2(OH)\}ClO_4$. $[Ga(TPP)(OH)]$ (54 mg, 77.2 μ mol) was dissolved in 20 mL of CH_2Cl_2 in a separatory funnel and titrated with a 17.2 mM solution of $HClO_4$. The mixture was vigorously shaken after each 200–500 μ L addition of titrant. The progress of the reaction was followed spectrophotometrically by diluting an aliquot (1 μ L) of the reaction mixture in *ca.* 2 mL of CH_2Cl_2 in a 1 cm path length cuvette; the intensity of the Soret band of $[Ga(TPP)(OH)]$ (420 nm) decreased relative to a new Soret band from $\{[Ga(TPP)]_2(OH)\}ClO_4$ at 399 nm. The concentration of $\{[Ga(TPP)]_2(OH)\}ClO_4$, as judged from the spectra of the dilute solutions used for the spectroscopic assay, reached a maximum after *ca.* 1.3 molar equivalents of acid (in the aqueous phase) had been added. Addition of excess acid resulted in the loss of the 399-nm band and the appearance of a new Soret band at 415 nm; the process was reversible upon addition of dilute NaOH solution. The titration was stopped when the intensity of the Soret band of $\{[Ga(TPP)]_2(OH)\}ClO_4$ (399 nm) was approximately 40% of that of the monomer, $[Ga(TPP)(OH)]$. The wine-red CH_2Cl_2 phase was separated, dried over anhydrous magnesium sulfate, filtered, and slowly concentrated on a rotary evaporator. Addition of hexane to the concentrated solution afforded a plum-colored precipitate which was isolated by filtration and washed with hexane. Spectroscopic data for $\{[Ga(TPP)]_2(OH)\}ClO_4$: IR (cm^{-1}): 1099(s) (ν_{ClO_4}). UV/vis (nm, CH_2Cl_2): λ_{max} 380 (N), 399 (Soret), 548, 591.

Synthesis of $\{[Al(OEP)]_2(OH)\}ClO_4$. The identical procedures of *Method 1* and *Method 2* for $\{[Ga(OEP)]_2(OH)\}ClO_4$ were applied for the synthesis of $\{[Al(OEP)]_2(OH)\}ClO_4$, starting from $[Al(OEP)(OH)]$. With *Method 1*, after ~0.5 equivalent of H^+ was introduced, a blue-shift of the Soret band (from 397 to 379 nm) was observed and a species with a Soret band at 379 nm became dominant in the reaction system. With *Method 2*, a species with a Soret band at 379 nm was also generated. Unfortunately, all attempted crystallizations of this interesting compound were unsuccessful.

Physical measurements

NMR spectroscopy. 1H , ^{13}C , and ^{71}Ga NMR spectra were recorded on Varian UNITYplus and Varian VXR–500S spectrometers operating at magnetic field strengths B_0 of 7.04 and 11.74 T, respectively. The experiments were carried out over a –40 to +90 °C temperature range using 1×10^{-5} to 7×10^{-7} M solutions in $CDCl_3$ (–40.0 to +30.0 °C) and $CDCl_2CDCl_2$ (+20.0 to +90.0 °C). Relatively low concentrations were used for

$\{[\text{Ga}(\text{OEP})_2(\text{OH})]\text{ClO}_4$ because of solubility limitations at lower temperatures. In the case of $\{[\text{Ga}(\text{TPP})_2(\text{OH})]\text{ClO}_4$, however, a 2.2×10^{-4} M solution in CDCl_3 was used to maximize the concentration of the dimer. DQF-COSY and NOESY (mixing time 300 ms) spectra were recorded in phase sensitive mode using standard pulse sequences [49, 50]. HETCOR experiments were performed using the pulse sequence described by Bax and Morris [51]. ^{13}C spin-lattice relaxation times, T_1 , were measured with proton decoupling using the inversion recovery technique [52]. At least fourteen different τ values were used and the waiting period between successive acquisitions was at least 2–3 times the longest T_1 time measured. The values of the relaxation times were obtained from three-parameter fits to the raw data [53]. $^{13}\text{C}\{^1\text{H}\}$ NOE enhancements were measured using gated decoupling techniques [54]. Chemical shifts are reported in δ (ppm) using TMS as an internal standard for all ^1H and ^{13}C spectra. The resonance signal of $\text{Ga}(\text{NO}_3)_3$ obtained in D_2O solution was used as an external standard for all ^{71}Ga NMR spectra.

Electrochemistry. Cyclic voltammetry (CV) experiments were performed using a Cypress System Model CS-1090 Computer-Controlled Electroanalytical System. Current-voltage curves were recorded on a HP Laser printer, or EPSON Model FX-850 printer. A three-electrode system was used with a platinum button working electrode, a platinum wire counter electrode, and a saturated calomel reference electrode (SCE). The solvent was dry, degassed CH_2Cl_2 containing 0.10 M TBAP as the supporting electrolyte. All CV experiments were conducted under an argon atmosphere.

Mass spectrometry. Fast Atom Bombardment (FAB) mass spectra were acquired with a JEOL JMS-AX505HA mass spectrometer. Xenon gas (>99.995% purity, Air Products) was used with the JEOL FAB gun which was operated at 5 kV primary beam energy and 10 mA emission current. The instrument was operated with an accelerating voltage of 3 kV and a resolution of 2000 (10% valley definition). Samples for mass spectrometry were prepared with 1–3 μL of a dichloromethane solution and were transferred to the FAB probe tip which had been coated with 2-nitrophenyloctyl ether (Sigma Grade, Sigma). Data were acquired over the mass range 500–1500 at 15 s/scan cycle or 500–2300 at 22 s/scan cycle. Results represent the average of 5–10 scans. Samples were initially dissolved in methylene chloride.

DFT simulations

DFT simulations at the HSEH1PBE [55]/SDD [56] level of theory (default convergence criteria and integration grid) were performed using 64-bit Gaussian 16W and GaussView 6. After initial structures were created in GaussView, their geometries were optimized to stationary points *in vacuo*. This was followed by a full frequency analysis to establish the nature of the stationary

point obtained and to generate all normal modes of vibration for the compound. NMR shielding tensors were calculated by the GIAO method without spin–spin interactions [57, 58]. Electronic spectra were calculated using the TD-DFT method of Bauernschmitt and Ahlrichs [59]; 75 singlet excited states were calculated in each case to generate the key spectral bands over a wide spectral range (down to $\lambda \sim 200$ nm for the highest energy excited states). Calculations were also performed in solvent continua (CDCl_3 or CH_2Cl_2) by fully optimizing the geometry of the complex in the solvent (SCRF PCM model) [60] prior to calculating the normal modes of vibration, NMR shielding tensors, and singlet excited states to permit accurate comparisons with experimental data. Fractional atomic charges were calculated using natural population analysis in NBO 3.0 [21], which gives distributions that are independent of the basis set employed for the calculations.

Simulations on $\{[\text{Ga}(\text{porphine})_2(\text{OH})]^+\}$ were attempted first. The refined geometry of the simplest member of the series was subsequently used to generate the input structure of $\{[\text{Ga}(\text{OEP})_2(\text{OH})]^+\}$ in which the ethyl group configurations of each ring were 4 *exo*/4 *endo* (++++– – –) as this configuration is common in several bridged $\text{M}(\text{OEP})$ complexes, including $\{[\text{In}(\text{OEP})_2(\text{OH})]^+\}$ [15]. The closest structure to those reported here, $\{[\text{Ga}(\text{OEP})_2(\text{OH})][\text{Ga}(\text{OEP})(\text{H}_2\text{O})]^+\}$ [15], however, has a 5 *exo*/3 *endo* configuration. Because rotation of the ethyl groups is likely facile in solution (giving averaged signals from the CH_2CH_3 groups), we averaged the shielding tensors of their constituent atoms to facilitate comparisons with experiment. Simulations on the congener, $\{[\text{Ga}(\text{TPP})_2(\text{OH})]^+\}$, were effected similarly.

All geometry optimizations converged on stable energy minima with non-imaginary normal modes of vibration, with the exception of the structure of $\{[\text{Ga}(\text{TPP})_2(\text{OH})]^+\}$ in a CHCl_3 solvent continuum, which converged on a stationary point with one imaginary frequency at -5.5 cm^{-1} . Examination of the vibrational mode indicated that it involved pure rotation about the $\text{N}_p\text{–Ga–Ga–N}_p$ dihedral angle. Based on the small magnitude of the eigenvalue and its nature, the calculated geometry was an acceptable solution phase minimum. All simulated spectra were plotted using spectral widths of 4 cm^{-1} (IR), 0.025 ppm (^1H NMR), and 2000 cm^{-1} (full-width at half-maximum, UV-vis), unless otherwise indicated.

X-ray structure determinations

The four crystal structure determinations were carried out on an Enraf-Nonius FAST area-detector diffractometer with a Mo rotating anode source ($\lambda = 0.71073$ Å). Our detailed methods and procedures for small molecule X-ray data collection with the FAST system have been described previously [61]. Data collections were performed at room temperature (20 ± 2 °C) for $[\text{In}(\text{OEP})_2(\text{OH})]$ and low temperature (-146 ± 2 °C) for the three

μ -hydroxo dimer structures. Crystal decay was excluded by comparison of the relative scale factors of individual *sweep* data [62]. Data were corrected for Lorentz and polarization factors and at the final stages of analysis, a modified version [63] of the absorption correction program DIFABS [64] was applied.

All four structures were solved using the direct methods program SHELXS [65]; subsequent difference Fourier syntheses led to the location of all the remaining nonhydrogen atoms. All structures were refined against F^2 with the program SHELXL [66] where all data collected were used, including negative intensities. Hydrogen atoms of the porphyrin ligands and the ordered solvent molecules were idealized with the standard SHELXL idealization methods; those belong to the disordered solvates were ignored. The hydroxo hydrogen atoms in $\{[\text{Ga}(\text{OEP})_2(\text{OH})]\text{ClO}_4$ and the triclinic polymorph of $\{[\text{In}(\text{OEP})_2(\text{OH})]\text{ClO}_4$ were directly located from the difference Fourier map and included in the least-squares refinement as isotropic contributors; however, the hydroxo hydrogen atoms in the monoclinic polymorph of $\{[\text{In}(\text{OEP})_2(\text{OH})]\text{ClO}_4$ and $[\text{In}(\text{OEP})(\text{OH})]$ could not be located.

Solvent disorder was observed in all three μ -hydroxo structures. For $\{[\text{Ga}(\text{OEP})_2(\text{OH})]\text{ClO}_4$, two CH_2Cl_2 molecules were found per asymmetric unit, one of which has two orientations: Cl(4)–C(2)–Cl(5a) and Cl(4)–C(2)–Cl(5b) with occupancies of 0.835 (8) and 0.165 (8) for Cl (5a) and Cl(5b), respectively. For triclinic $\{[\text{In}(\text{OEP})_2(\text{OH})]\text{ClO}_4$, there are two independent μ -hydroxo molecules (*A* and *B*) in the asymmetric unit and a total of three toluene molecules, two water molecules, and one methylene chloride molecule as solvent components. Among these solvent molecules, two of the three toluene molecules and one water molecule were ordered and fully occupied, the remaining species were only partially present. One of the two perchlorate anions was disordered at two positions (*a* and *b*). Based on consideration of the non-bonding interactions, the perchlorate disorder was judged to be associated with the partial occupancy of the solvent components. Thus, refinement of group occupancies was applied, which led to occupancy factors 0.663 (3) for perchlorate (*a*) and the partial toluene molecule, 0.337 (3) for perchlorate (*b*) and the partial CH_2Cl_2 molecule. The occupancy for the partial water molecule (O(w2)) was refined independently to be 0.18 (2). For monoclinic $\{[\text{In}(\text{OEP})_2(\text{OH})]\text{ClO}_4$, three toluene molecules and one water molecule were found in the asymmetric unit with each μ -hydroxo dimer. Two of the three toluene molecules have an inversion center at the center of the six-membered ring, and thus they are equally shared between two asymmetric units. The water molecule was disordered at two positions, O(w1) and O(w2) with occupancy factors of 0.46(3) and 0.54(3), respectively. Rigid-group descriptions were applied for the disordered toluene molecules in both $\{[\text{In}(\text{OEP})_2(\text{OH})]\text{ClO}_4$ structures.

Crystal data for the four structures are listed in Table S5. Complete crystallographic details, anisotropic thermal parameters and the fixed hydrogen atom coordinates are available as CIF files (Supporting Information).

SUMMARY AND CONCLUSIONS

The synthesis, solution and solid-state characterization of 5-coordinate Group 13 (aluminum, gallium, and indium) metalloporphyrin hydroxide derivatives are reported. These derivatives include both the monomeric $[\text{M}(\text{OEP})(\text{OH})]$ species and their dinuclear $\{[\text{M}(\text{OEP})_2(\text{OH})]\}^+$ counterparts. The mononuclear $[\text{In}(\text{OEP})(\text{OH})]$ complex has been structurally characterized by single crystal X-ray diffraction and spectroscopy. The reaction of the 5-coordinate monomeric hydroxides in CH_2Cl_2 with a slight stoichiometric excess of aqueous perchloric acid permits the synthesis of the 5-coordinate μ -hydroxo-bridged complexes $\{[\text{M}(\text{Porph})_2(\text{OH})]\text{ClO}_4$ *via* loss of water (condensation). The μ -hydroxo dimers were characterized by ^1H , ^{13}C , and ^{71}Ga NMR spectroscopy, UV-vis spectra, electrochemistry, and X-ray structure determinations of the gallium(III) and indium(III) OEP derivatives. DFT simulations afforded suitable solution phase structures (geometries) and signature spectroscopic features (NMR shielding tensors, IR vibrational modes, and electronic spectra) for the experimentally-characterized mono- and dinuclear derivatives. The DFT-calculated frontier MOs (FMOs) of the μ -hydroxo dimers (localized on the porphyrin macrocycles) accounted for both their redox behavior and stability in solution. Finally, TD-DFT calculated electronic spectra confirmed the nature of the species involved in the synthetic equilibrium for the Ga(III) OEP derivatives; six-coordinate $[\text{Ga}(\text{OEP})(\text{OH})_2]^+$ serves as the key intermediate in the conversion of $[\text{Ga}(\text{OEP})(\text{OH})]$ to $\{[\text{Ga}(\text{OEP})_2(\text{OH})]\text{ClO}_4$.

Acknowledgments

We thank the National Institutes of Health for support of this research under Grant GM-38401. We thank Dr. Bill Boggess of the Mass Spectrometry Facility and Mr. Don Schifferl of the NMR Spectrometry Facility for assistance (University of Notre Dame). Funds for the purchase of the FAST area detector diffractometer were provided through NIH Grant RR-06709 to the University of Notre Dame. Part of this work was funded by the South African Research Chairs Initiative of the Department of Science and Technology and National Research Foundation of South Africa (Grant No 64799 to OQM).

Supporting information

Electronic spectra monitoring the conversion of monomeric $[\text{Ga}(\text{OEP})(\text{OH})]$ to $\{[\text{Ga}(\text{OEP})_2(\text{OH})]\text{ClO}_4$. Electronic spectra illustrating the difference in the Soret

band for the starting material [In(OEP)(OH)], the “aqua” complex, {[In(OEP)₂(OH)}ClO₄ and the analogous aluminum species. Mean plane diagrams for the two rings of {[In(OEP)₂OH⁺} and an ORTEP view of [In(OEP)(OH)]. Atomic coordinates of DFT-optimized structures, DFT-calculated electronic spectra, and chemical shift correlations. Tables S1–S5 give experimental and DFT calculated ¹³C NMR, ¹³C spin relaxation times, ¹³C NOE parameters, frontier molecular orbital energies and crystallographic data and collection parameters. Crystallographic data have been deposited at the Cambridge Crystallographic Data Centre (CCDC) under numbers CCDC 1904457 and CCDC 1904459–1904461 (four CIF files). Copies can be obtained on request, free of charge, via www.ccdc.cam.ac.uk/data-request/cif or from the Cambridge Crystallographic Data Centre, 12 Union Road, Cambridge CB2 1EZ, UK (fax: +441223-336-033 or email: deposit@ccdc.cam.ac.uk).

REFERENCES

- Buchler JW, De Cian A, Fischer J, Kihn-Botulinski M, Paulus H and Weiss R. *J. Am. Chem. Soc.* 1986; **108**: 3652–3659.
- Schaverien CJ and Orpen AG. *Inorg. Chem.* 1991; **30**: 4968–4978.
- Buchler JW, De Cian A, Fischer J, Hammerschmitt P, Löffler J, Scharbert B and Weiss R. *Chem. Ber.* 1989; **122**: 2219–2228.
- Gross T, Chevalier F and Lindsey JS. *Inorg. Chem.* 2001; **40**: 4762–4774.
- Buchler JW, De Cian A, Fischer J, Hammerschmitt P and Weiss R. *Chem. Ber.* 1991; **124**: 1051–1058.
- Bertini I, Coutsolelos A, Dikiy A, Luchinat C, Spyroulias GA and Troganis A. *Inorg. Chem.* 1996; **35**: 6308–6315.
- Collman JP and Arnold HJ. *Acc. Chem. Res.* 1993; **26**: 586–592.
- Daphnomili D, Raptopoulou C, Terzis A, Agondanou JH, Bénazeth S and Coutsolelos A. *Inorg. Chem.* 2004; **43**: 4363–4371.
- Scheidt WR, Cheng B, Safo MK, Cukiernik F, Marchon J-C and Debrunner PG. *J. Am. Chem. Soc.* 1992; **114**: 4420–4421.
- Abbreviations: M, metal ion; OEP and TPP are the dianions of octaethylporphyrin and tetraphenylporphyrin, respectively; Porph, generic porphyrin dianion; FWHM, full width at half maximum; SCE, saturated calomel electrode; TBAP, tetrabutylammonium perchlorate (supporting electrolyte); TMS, tetramethyl silane; TFPB, tetrakis[3,5-bis-(trifluoromethyl)phenyl]borate; DQF-COSY, Double-Quantum Filtered Correlated Spectroscopy; NOESY, Nuclear Overhauser Spectroscopy; HETCOR, Heteronuclear Chemical-Shift Correlation; DFT, density functional theory; GIAO, gauge independent atomic orbital.
- Cheng B, Cukiernik F, Fries PH, Marchon J-C and Scheidt WR. *Inorg. Chem.* 1995; **34**: 4627–4639.
- Cheng B, Fries PH, Marchon J-C and Scheidt WR. *Inorg. Chem.* 1996; **35**: 1024–1032.
- Cheng B, Hobbs JD, Debrunner PG, Erlebacher J, Shelnutz JA and Scheidt WR. *Inorg. Chem.* 1995; **34**: 102–110.
- Guchhait T, Sasmal S, Khan FST and Rath S P. *Coord. Chem. Rev.* 2017; **337**: 112–144.
- Parzuchowski PG, Kampf JW, Różniecka E, Kondratenko Y, Malinowska E and Meyerhoff ME. *Inorg. Chim. Acta*, 2003; **355**: 302–313.
- Furhop JH, Kadish KM and Davis DG. *J. Am. Chem. Soc.* 1973; **95**: 5140–5147.
- Shannon RD. *Acta Cryst. Sect. A*, 1976; **32**: 751–767.
- Gouterman M, Wagnière GH and Snyder LC. *J. Mol. Spectros.* 1963; **11**: 108–127.
- Weiss C, Kobayashi H and Gouterman M. *J. Mol. Spectros.* 1965; **16**: 415–450.
- Pinter TB, Dodd EL, Bohle DS and Stillman MJ. *Inorg. Chem.* 2012; **51**: 3743–3753.
- Reed AE, Weinstock RB and Weinhold F. *J. Chem. Phys.* 1985; **83**: 735–746.
- Durand Jr RR, Bencosme CS, Collman JP and Anson FC. *J. Am. Chem. Soc.* 1983; **105**: 2710–2718.
- Kadish K, Cornillon J, Coutsolelos A and Guillard R. *Inorg. Chem.* 1987; **26**: 4167–4173.
- Cardona CM, Li W, Kaifer AE, Stockdale D and Bazan GC. *Advanced Materials* 2011; **23**: 2367–2371.
- Elschner A, Heuer HW, Jonas F, Kirchmeyer S, Wehrmann R and Wussow K. *Advanced Materials* 2001; **13**: 1811–1814.
- Hamada Y, Kanno H, Sano T, Fujii H, Nishio Y, Takahashi H, Usuki T and Shibata K. *Appl. Phys. Lett.* 1998; **72**: 1939–1941.
- Ragoussi ME and Torres T. *Chem. Commun.* 2015; **51**: 3957–3972.
- Wannere CS and Schleyer PVR. *Organic Lett.* 2003; **5**: 605–608.
- Eaton S, Fishwild D and Eaton G. *Inorg. Chem.* 1978; **17**: 1542–1545.
- Lux D, Daphnomili D and Coutsolelos A. *Polyhedron* 1994; **13**: 2367–2377.
- Coutsolelos A, Lux D and Mikros E. *Polyhedron* 1996; **15**: 705–715.
- Abraham A and Smith K. *Tetrahedron Lett.* 1971; **12**: 3335–3338.
- Coutsolelos A, Guillard R, Bayeul D and Lecomte C. *Polyhedron* 1986; **5**: 1157–1164.
- Busby CA and Dolphin D. *J. Magn. Reson.* (1969) 1976; **23**: 211–220.
- Abraham A. *The Principles of Nuclear Magnetism*, Oxford University Press, Oxford, 1961.
- Doddrell D, Glushko V and Allerhand A. *J. Chem. Phys.*, 1972; **56**: 3683–3689.

37. London RE. *Magnetic Resonance in Biology*, John Wiley and Sons, Vol. 1, New York, 1980.
38. Craig AS, Parker D, Adams H and Bailey NA. *J. Chem. Soc., Chem. Commun.* 1989; 1793–1794.
39. Prata M, Santos A, Geraldés C and De Lima J. *J. Inorg. Biochem.* 2000; **79**: 359–363.
40. Lowe MP, Rettig SJ and Orvig C. *J. Am. Chem. Soc.* 1996; **118**: 10446–10456.
41. Császár AG, Czakó G, Furtenbacher T, Tennyson J, Szalay V, Shirin SV, Zobov NF and Polyansky L. *J. Chem. Phys.* 2005; **122**: 214305.
42. Bacon G. *Acta Crystallogr.* 1951; **4**: 558–561.
43. Scheidt WR and Lee Y. *Struct. Bonding* 1987; **64**: 1–70.
44. Jentzen W, Ma JG and Shelnutz JA. *Biophys. J.* 1998; **74**: 753–763.
45. Adler AD, Longo FR, Finarelli JD, Goldmacher J, Assour J and Korsakoff L. *J. Org. Chem.* 1967; **32**: 476.
46. Wolsey WC. *J. Chem. Educ.* 1973; **50**: A335.
47. Kaizu Y, Misu N, Tsuji K, Kaneko Y and Kobayashi H. *Bull. Chem. Soc. Japan* 1985; **58**: 103–108.
48. Bhatti M, Bhatti W and Mast E. *Inorg. Nucl. Chem. Lett.* 1972; **8**: 133–137.
49. Rance M, Sørensen O, Bodenhausen G, Wagner G, Ernst R and Wüthrich, K. *Biochem. Biophys. Res. Commun.* 1983; **117**: 479–485.
50. Bodenhausen G, Kogler H and Ernst R. *J. Magn. Reson.* 1984; **58**: 370–388.
51. Bax A and Morris GA. *J. Magn. Reson.* 1981; **42**: 501–505.
52. Martin M, Delpuech J and Martin G. *Practical NMR Spectroscopy*, Heyden & Son Ltd, London, 1980.
53. Weiss GH and Ferretti JA. *Progr. Nucl. Magn. Reson. Spectr.* 1988; **20**: 317–335.
54. Neuhaus D and Williamson M. *The Nuclear Overhauser Effect in Structural and Conformational Analysis*, VCH: New York, 1989, pp. 51–56.
55. Heyd J and Scuseria GE. *J. Chem. Phys.* 2004; **121**: 1187–1192.
56. Fuentealba P, Preuss H, Stoll H and Vón Szentpály L. *Chem. Phys. Lett.* 1982; **89**: 418–422.
57. Ruud K, Helgaker T, Bak KL, Jorgensen P and Jensen HJA. *J. Chem. Phys.* 1993; **99**: 3847–3859.
58. Cheeseman JR, Trucks GW, Keith TA and Frisch MJ. *J. Chem. Phys.* 1996; **104**: 5497–5509.
59. Bauernschmitt R and Ahlrichs R. *Chem. Phys. Lett.* 1996; **256**: 454–464.
60. Miertuš S, Scrocco E and Tomasi J. *Chem. Phys.* 1981; **55**: 117–129.
61. Scheidt WR and Turowska-Tyrk I. *Inorg. Chem.* 1994; **33**: 1314–1318.
62. Carrell HL. SCALEXPRO, The Institute for Cancer Research, Fox Chase Cancer Center, USA. The program SCALEXPRO was used to calculate the relative scale factors for each *sweep* data set.
63. Karaulov AI. School of Chemistry and Applied Chemistry, University of Wales, Cardiff CF1 3TB, UK, *Personal Communication*. The process is based on an adaptation of the DIFABS [64] logic to area detector geometry.
64. Walker N and Stuart D. *Acta Crystallogr. Sect. A*, 1983; **39**: 158–166.
65. Sheldrick GM. *Acta Crystallogr. Sect. A*. 2008; **64**: 112–122.
66. Sheldrick GM. *Acta Crystallogr. Sect. C*. 2015; **71**: 3–8.